JCI The Journal of Clinical Investigation

MOGAT3-Mediated DAG Accumulation Drives Acquired Resistance to Anti-BRAF/EGFR Therapy in BRAFV600E-Mutant Metastatic Colorectal Cancer

Jiawei Wang, … , Zhenyu Ju, Zhangfa Song

J Clin Invest. 2024. https://doi.org/10.1172/JCI182217.

Research In-Press Preview Gastroenterology Therapeutics

Graphical abstract

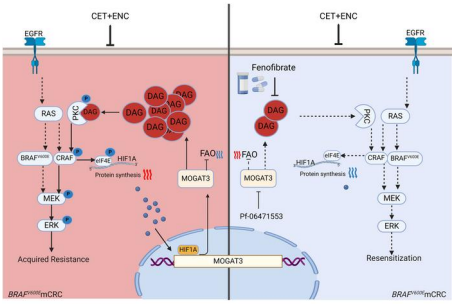

MOGAT3-Mediated DAG Accumulation Drives Acquired Resistance to Anti-BRAF/EGFR Therapy in *BRAF*^{V600E}-Mutant Metastatic Colorectal Cancer

Jiawei Wang[1,2,3,6], Huogang Wang[1,2,3,6], Wei Zhou[1,2,3], Xin Luo[1], Huijuan Wang[1,2,3], Qing Meng[1,2,3], Jiaxin Chen[1], Xiaoyu Chen[1,2,3], Yingqiang Liu[1,2,3], David W Chan[4], Zhenyu Ju[5], Zhangfa Song[1,2,3#]

[1] Department of Colorectal Surgery, Sir Run Run Shaw Hospital, School of Medicine, Zhejiang University, Hangzhou, Zhejiang, 310016, P.R. China.

[2] Key Laboratory of Biological Treatment of Zhejiang Province, 310016, Hangzhou, P.R. China

[3] Key Laboratory of Integrated Traditional Chinese and Western Medicine Research on Anorectal Diseases of Zhejiang Province,310016, Hangzhou, P.R. China.

[4] School of Medicine, The Chinese University of Hong Kong, Shenzhen, Guangdong, 518172, P.R. China.

[5] Key Laboratory of Regenerative Medicine of Ministry of Education, Institute of Aging and Regenerative Medicine, Jinan University, Guangzhou, P.R. China

[6] These authors contributed equally: Jiawei Wang, Huogang Wang.

#Correspondence should be addressed to:

Prof. Zhangfa Song, Department of Colorectal Surgery, Sir Run Run Shaw Hospital, Zhejiang University School of Medicine, Key Laboratory of Biological Treatment of Zhejiang Province, Key Laboratory of Integrated Traditional Chinese and Western

Medicine Research on Anorectal Diseases of Zhejiang Province, 310016, Hangzhou, China. Phone: (86) 571-86006355; E-mail: songzhangfa@zju.edu.cn

Authorship note: JW and HW contributed equally to this work

Authors' Disclosures: The authors have declared that no conflict of interest exists.

Abstract

BRAF^{V600E}-mutant metastatic colorectal cancer (mCRC) is associated with poor prognosis. The combination of anti-BRAF/EGFR (encorafenib/cetuximab) treatment for patients with *BRAF*^{V600E}-mutant mCRC improves clinical benefits; unfortunately, inevitable acquired resistance limits the treatment outcome, and the mechanism has not been validated. Here, we discovered that monoacylglycerol O-Acyltransferase 3 (MOGAT3) mediated diacylglycerol (DAG) accumulation contributed to acquired resistance to encorafenib/cetuximab by dissecting *BRAF*^{V600E}-mutant mCRC patient-derived xenograft (PDX) model exposed to encorafenib/cetuximab administration. Mechanistically, the upregulated MOGAT3 promotes DAG synthesis and reduces fatty acid oxidation (FAO)-promoting DAG accumulation and activating PKCα-CRAF-MEK-ERK signaling, driving acquired resistance. Resistance-induced hypoxia promotes MOGAT3 transcriptional elevation; simultaneously, MOGAT3-mediated DAG accumulation increases HIF1A expression in translation level through PKCα-CRAF-eIF4E activation, strengthening the resistance status. Intriguingly, reducing intratumoral DAG by fenofibrate or Pf-06471553 restores the antitumor efficacy of encorafenib/cetuximab on resistant *BRAF*^{V600E}-mutant mCRC, interrupted PKCα-CRAF-MEK-ERK signaling. These findings reveal the critical role of metabolite DAG as a modulator of encorafenib/cetuximab efficacy in *BRAF*^{V600E}-mutant mCRC, suggesting that fenofibrate might prove beneficial for resistant *BRAF*^{V600E}-mutant mCRC patients.

Introduction

Colorectal cancer (CRC), the second-leading cause of cancer-related mortality worldwide, is a highly heterogeneous cancer with multiple genetic subtypes (1). 10 % of CRC patients are diagnosed with mutations in the *BRAF* oncogene of the MAPK pathway, and the most common missense mutation occurs at the 600th amino acid with a valine to glutamic acid (V600E), predicating distant metastasis and poor prognosis (2). Unfortunately, the patients diagnosed with metastatic CRC (mCRC) harboring $BRAF^{V600E}$-mutant poorly respond to conventional chemotherapy (3). Recently, anti-BRAF/EGFR combinatorial therapy (encorafenib/cetuximab) was approved in April 2020 by the U.S. Food and Drug Administration (FDA) for the treatment of patients with $BRAF^{V600E}$-mutant mCRC (4). Despite the favorable initial response of this therapy, almost all the $BRAF^{V600E}$-mutant mCRC patients developed therapy resistance after approximately 4.3 months of treatment (5). Moreover, the objective response rate was only 28.0%, and the median overall survival (OS) was 9.57 months (6). Improving the efficiency of encorafenib/cetuximab to control disease progression on $BRAF^{V600E}$-mutant mCRC remains challenging.

Co-targeting BRAF/EGFR reinforces inhibition of the oncogenic BRAF-MEK pathway while shutting down the adverse feedback resistance pathway (EGFR), the theoretical basis of dual-target therapy. A recent study showed that SRC kinases are systematically activated in $BRAF^{V600E}$-mutant CRC following targeted inhibition of BRAF ± EGFR (7). Clinical observation showed that 43% of $BRAF^{V600E}$ CRC patients treated with anti-BRAF/EGFR obtained *RNF43* mutation related to treatment failure

(8). Continuous treatment often drives genomic alteration or epigenetic changes, ultimately leading to resistance. However, the acquired resistance mechanism of $BRAF^{V600E}$-mutant mCRC to encorafenib/cetuximab ongoing treatment is largely unknown.

Metabolic adaptation confers tumors surviving in a harsh drug-exposure environment (9), especially in $BRAF^{V600E}$-mutant tumors (10). The preclinical model evidenced that $BRAF^{V600E}$-mutant tumors determine lipid profiles against drug treatment (11). In addition to fueling tumor cells, lipids orchestrate signal transduction cascades to support tumor growth upon harsh drug treatment. Moreover, increasing evidence indicated that aberrant lipid droplet (LD) accumulation in CRC with *KRAS* and *BRAF* mutation is associated with a poor response to anti-EGFR therapy (erlotinib), implying drug-resistance status in *BRAF* mutated tumors is closely related to lipid metabolism (12) (13). As an essential lipid metabolism pathway, glyceride homeostasis maintains various biological processes and functions, including energy supply and signal transduction (14), primarily dependent on monoacylglycerol acyltransferase (MOGAT) activity (15). Abnormal MOGAT enzyme activities (MOGAT1, MOGAT2, and MOGAT3) are associated with various disease progressions, such as nonalcoholic fatty liver disease (NAFLD) and obesity (16, 17). Similarly, *MOGAT3* is believed to maintain glyceride homeostasis in the human intestine and liver (18); however, the functions of *MOGAT3* on physiological processes and tumor progression remain to be clarified.

In this study, we reported that the upregulated MOGAT3 endows resistance status

of *BRAF*^{V600E}-mutant mCRC to encorafenib/cetuximab treatment through synthesis diacylglycerol (DAG), connecting PKCα-CRAF-MEK-ERK signaling axis. Specifically, resistance-induced hypoxia promotes *MOGAT3* transcriptional elevation and MOGAT3-mediated DAG synthesis and inhibits lipid oxidation respiration, resulting in intratumoral DAG accumulation. Accumulated intratumoral DAG re-activates MAPK signaling circuitry through PKCα-CRAF phosphorylation activation and strengthens HIF1A expression through PKCα-CRAF-eIF4E activation. Of note, targeting MOGAT3 or reducing intratumoral DAG restores the treatment efficiency of anti-BRAF/EGFR combinatorial therapy in resistant *BRAF*^{V600E}-mutant mCRC. Overall, our study uncovers a clinically actionable strategy to fix the failure of anti-BRAF/EGFR combinatorial therapies.

Results

Upregulated Lipid Metabolism Linked to Encorafenib/Cetuximab Resistance in *BRAF*^{V600E}-mutant mCRC

To investigate the potential mechanism of the acquired resistance of anti-BRAF/EGFR therapy to *BRAF*^{V600E}-mutant mCRC, we first employed operative tumor tissue derived from untreated *BRAF*^{V600E}-mutant colorectal cancer patient with liver metastasis to establish patient-derived xenograft (PDX) models to thoroughly assesses the progressive resistance of encorafenib/cetuximab treatment on *BRAF*^{V600E}-mutant mCRC (Figure 1A). The histological assessment showed successful PDX tumor model establishment (Supplemental Figure 1A). PDX tumors reaching 150 mm^3 received either vehicle or drug treatments (20 mg/kg encorafenib orally daily; 20 mg/kg cetuximab *i.p.* injection twice weekly), mirroring clinical dosing (19). After continuous dosing, tumors exhibited resistance compared to initial regression (Figure 1B). The response of PDX tumors to encorafenib/cetuximab treatment was categorized into three stages based on tumor volume changes: baseline (untreated), sensitive (regression from baseline), and resistant (progression from baseline) (Figure 1B). Moreover, histological analysis of PDX tumors revealed statistically significant increases in Ki67 levels and decreases in TUNEL levels in resistant tumors compared to sensitive ones after 20 days of encorafenib/cetuximab treatment (Supplemental Figure 1A). Notably, resistant PDX tumors recapitulated the response to encorafenib/cetuximab treatment in vivo, confirming the successful establishment of the acquired resistant PDX model (Supplemental Figure 1C). Sensitive and resistant

PDX tumors were then re-implanted in vivo. After 20 days of drug-free growth, both were subjected to encorafenib/cetuximab therapy. The resistant tumors maintained their robust resistance, demonstrating that the resistance in the PDX model is stable and enduring, not merely a transient adaptive response (Supplemental Figure 1D). To characterize *BRAF*^{V600E}-mutant mCRC evolution to anti-BRAF/EGFR therapy, we first performed whole exome sequencing (WES) to analyze the PDX tumors within different response periods (baseline, sensitive, and resistant). *BRAF*^{V600E}-mutant was conserved, and no new consistent mutations (e.g., *RNF43*) were detected in resistant tumors compared to baseline and sensitive ones, suggesting that transcriptional differences may underlie the acquired resistance (Supplemental Figure 1B). Next, transcriptomic analysis was performed to compare the PDX tumors in baseline, sensitive, and resistant periods. The RNA-seq enrichment analysis identified that the most differentially regulated pathway was the metabolic pathway (Figure 1, C and D), especially the lipid metabolism pathway (Figure 1E), which significantly upregulated in resistant tumors. Moreover, gene set enrichment analysis (GSEA) revealed that the lipid metabolic process upregulated in resistant PDX tumors (Figure 1F). Consistently, we observed that the levels of intratumoral lipid (identified by Nile Red staining) markedly increased in resistant PDX tumor tissues compared with sensitive PDX tumors (Figure 1G). In addition, we generated two encorafenib/cetuximab-resistant human *BRAF*^{V600E}-mutant CRC cell lines, RKO EC-R and HT29 EC-R (Supplemental Figure 1E). Similar intracellular lipids increase was observed in resistant cells (identified by BODIPY 493/503 staining), and *BRAF*^{V600E} mutation was consistent in

157 resistant cells and parental cells (Figure 1H and Supplemental Figure 1F). Together,
158 these results suggested lipid metabolism upregulation is associated with the acquired
159 resistance of anti-BRAF/EGFR therapy in *BRAF*^{V600E}-mutant CRC.
160
161 **DAG Accumulation Induces BRAF/EGFR Therapy Resistance in *BRAF*^{V600E}-**
162 **mutant mCRC**
163 To characterize the underlying lipid biological processes in the resistant
164 *BRAF*^{V600E}-mutant mCRC during dual therapy treatment, we performed lipid
165 metabolomics analysis and found that the glyceride metabolism process significantly
166 upregulated in resistant *BRAF*^{V600E}-mutant mCRC (Figure 2A). Glyceride metabolism
167 cycling is the process of diacylglycerols (DAGs), triacylglycerols (TAGs) synthesis
168 and decomposition (20). Indeed, we observed statistically significant increases in
169 intratumoral DAG and TAG levels in resistant PDX tumors compared to sensitive
170 ones (Figure 2B and Supplemental Figure 2, A-C). Further, we sorted Epcam^{+} tumor
171 cells from resistant and sensitive PDX tumors and discovered that DAG and TAG
172 predominantly originated from these cells (Supplemental Figure 2F). These results
173 suggest that elevated levels of TAG or DAG may contribute to the resistance observed.
174 To test this hypothesis, we first assessed the treatment efficiency of encorafenib
175 (0.25μM)-cetuximab (0.5μM) in sensitive RKO and HT29 cells upon DAG (10μM) or
176 TAG (10μM) treatment according to DAG/TAG concentration in resistant tumors.
177 Surprisingly, a significant increase in cell growth and decreased cell apoptosis was
178 observed in encorafenib/cetuximab plus DAG but not in the TAG group compared to

the doublet group (Supplemental Figure 2, D and E). These data demonstrated that DAG, but not TAG, enhances the resistance of *BRAF*^{V600E}-mutant mCRC to encorafenib/cetuximab.

To further substantiate DAG-mediated encorafenib/cetuximab resistance, we evaluated the treatment efficiency of encorafenib/cetuximab combined with DAG or vehicle in sensitive PDX tumors (Figure 2C). As expected, the DAG (100mg/kg/day) treatment significantly promoted sensitive PDX tumor growth upon doublet treatment, associated with intratumoral DAG elevation (Figure 2, C-F). Moreover, histological assessment of sensitive PDX tumors demonstrated statistically significant increases in the levels of Ki67 and decreased the TUNEL level upon DAG plus encorafenib/cetuximab treatment compared to the doublet group (Figure 2, G-H). These data illustrated that intratumoral DAG accumulation contributes to anti-BRAF/EGFR treatment resistance in *BRAF*^{V600E}-mutant mCRC.

MOGAT3-Driven DAG Buildup Promotes Anti-BRAF/EGFR Therapy Resistance

Next, we sought to elucidate the mechanism underlying intratumoral DAG accumulation in resistant *BRAF*^{V600E}-mutant mCRC. Diacylglycerol synthase *MOGAT3* (Supplemental Figure 3A), the only upregulated gene in both the Metabolic and Diacylglycerol O-acyltransferase pathway (Supplemental Figure 3E), was found upregulated dramatically in resistant PDX tumors and RKO EC-R cells (Supplemental Figure 3, B and D). Previous studies indicated that MOGAT activities catalyze the

synthesis of diacylglycerol from 2-monoacylglycerol and fatty acyl-CoA in the intestine (18, 21). Next, we observed MOGAT3 but not MOGAT1 or MOGAT2 markedly elevated in resistant PDX tumors and RKO EC-R cells compared to respective sensitive tumor cells (Figure 3A, Supplemental Figure 3C). Moreover, the protein level of MOGAT3 in parental RKO and HT29 cells was assessed upon monotherapy treatment (encorafenib or cetuximab). The western blot result showed MOGAT3 protein expression level was not changed upon monotherapy treatment, implying the acquired resistance of $BRAF^{V600E}$-mutant mCRC to doublet therapy responsible for MOGAT3 dysregulation (Supplemental Figure 3F). Next, we treated sensitive cells with encorafenib and cetuximab and assessed MOGAT3 protein levels. At the beginning of doublet inducing, MOGAT3 protein levels showed no change in sensitive cells (RKO and HT29 cell lines). Under continuous pressure of doublet therapy, MOGAT3 decreased was restored (Supplemental Figure 3G). These results suggested that long-term induction of sensitive cells might induce an increase in MOGAT3. We next examined whether MOGAT3-mediated DAG accumulation drives anti-BRAF/EGFR therapy resistance. Knocking out MOGAT3, in combination with encorafenib/cetuximab treatment, significantly inhibited RKO EC-R and HT29 EC-R cell growth and lowered DAG accumulation (Figure 3B and Supplemental Figure 3H). Moreover, knockout MOGAT3 in parental cells (RKO or HT29) showed no effect on cell proliferation (Supplemental Figure 3I). Similar to the in vitro results, knocking out MOGAT3 in RKO EC-R cells restored the efficacy of encorafenib/cetuximab treatment in Cell Line Derived Xenograft (CDX) tumors in vivo and reduced

intratumoral DAG levels compared to the doublet treatment group (Figure 3, C-E). Treatment with DAG alone did not affect tumor growth (Figure 3, C and E). In contrast, restoring DAG levels reversed the increased sensitivity to encorafenib/cetuximab treatment caused by MOGAT3 knockout in resistant tumors, leading to renewed CDX tumor growth (Figure 3, C-E). This suggests that the response to the doublet therapy is contingent upon intratumoral DAG levels. Moreover, histological analysis of RKO EC-R CDX tumors revealed a statistically significant decrease in Ki67 expression and an increase in TUNEL-positive cells in the MOGAT3 knockout group treated with encorafenib/cetuximab compared to the doublet treatment group, effects that were negated by DAG treatment (Supplemental Figure 3, J and K). Further, we assessed whether overexpressed MOGAT3 in sensitive RKO cells (OE-MOGAT3 RKO) would confer resistance to anti-BRAF/EGFR therapy in these cells. The tumor volume in the OE-MOGAT3 RKO CDX group increased approximately 4-fold compared to the NC-RKO CDX group when treated with encorafenib/cetuximab in vivo (Figure 3, F and H). Intratumoral DAG levels were statistically higher in OE-MOGAT3 RKO CDX tumors, aligning with the pattern observed in resistant tumors (Figure 3G). Histological assessment revealed a statistically significant rise in Ki67 and a reduction in TUNEL in OE-MOGAT3 RKO CDX tumors, indicating that MOGAT3-mediated DAG accumulation may confer resistance to $BRAF^{V600E}$ mutant mCRC (Supplemental Figure 3L). Next, we evaluated the impact of the MOGAT3 inhibitor PF-06471553 (Pf) on enhancing the efficacy of encorafenib/cetuximab in acquired resistant PDX tumors. The triplet combination led

to a roughly one-fold decrease in tumor volume and an approximate 2.5-fold reduction in intratumoral DAG levels in resistant PDX tumors relative to the doublet control group (Figure 3, I-K). Monotherapy of Pf reduced the intratumoral DAG but did not affect resistant PDX tumor growth, suggesting that MOGAT3-regulated levels of intratumoral DAG determine the treatment response of doublet therapy (Figure 3, I-K). Histological assessment of resistant PDX tumors demonstrated statistically decreased levels of Ki67 and increased TUNEL in the triplet regimen group compared to the doublet or monotherapy treatment group (Supplemental Figure 3M). In addition, MOGAT3 inhibitor Pf combined encorafenib/cetuximab reduced DAG and had an equivalent effect on growth inhibition in RKO EC-R and HT-29 EC-R cells (Supplemental Figure 3, N and O). Furthermore, triple therapy (BRAF+EGFR+MOGAT3 inhibitor) markedly increased apoptotic rates and the expression of pro-apoptotic proteins BAX and cleaved-Caspase3/9, while it decreased the expression of the anti-apoptotic protein Bcl2, compared to doublet therapy (Supplemental Figure 3, P and Q). Due to MOGAT3 being a pseudogene in mouse models, toxicity experiments were performed in rat models. Pf toxicity showed negligibility in the rat blood index and histopathology (including heart, liver, kidney, and lung) (Supplemental Figure 3, R and S). These results demonstrated that targeting MOGAT3 overcomes the resistance of $BRAF^{V600E}$-mutant mCRC to anti-BRAF/EGFR therapy by reducing intratumoral DAG.

MOGAT3 Inhibition Disrupts DAG Synthesis and Boosts Lipid-OXPHOS,

Lowering Intratumoral DAG

Next, we examined the functions of MOGAT3 in regulating DAG synthesis in resistant $BRAF^{V600E}$-mutant CRC cells. It has been reported that DAG synthesis relied on two pathways: the sn-glycerol-3-phosphate (G3P) pathway and the MOGAT-dependent pathway (22) (Figure 4B). We observed that LPIN1, the key to DAG synthesis in the G3P pathway, was unchanged in RKO and RKO EC-R cells, suggesting DAG synthesis is predominantly MOGAT3-dependent (Figure 4A). Further, we assessed the live-cell oxygen consumption rate (OCR) to profile the respiration of RKO and RKO EC-R cells and to ascertain if mitochondrial respiration is influenced by MOGAT3-mediated DAG accumulation. The Basal, Maximal, and ATP-linked OCR analyses indicated a significantly reduced OCR in RKO EC-R cells compared to RKO cells, suggesting inhibited oxidative phosphorylation in drug-resistant cells (Figure 4, D and E).

On the other hand, knockout of MOGAT3 did not affect LPIN1 protein levels in RKO EC-R cells, suggesting MOGAT3 regulates DAG synthesis in resistant CRC (Supplemental Figure 4A). Moreover, the level of intratumoral DAG decreased in the $MOGAT3^{KO}$ CDX group (Figure 4C), and the lipidomic analysis showed that MOGAT3 inhibition significantly reduced DAG-related lipid profiles in RKO EC-R cells (Supplemental Figure 4B). Additionally, Basal, Maximal, and ATP-linked OCR increased in MOGAT3 knockout RKO EC-R cells relative to the control group (Figure 4, F and G). We examined FAO in RKO EC-R cells to determine if MOGAT3-regulated OCR stems from Fatty Acid Oxidation (FAO). O2 consumption

decreased with etomoxir treatment in both RKO EC-R and RKO cells, with RKO EC-R cells showing lower O_2 consumption than RKO cells upon etomoxir treatment (Figure 4H). Moreover, there is a decrease in both basal and maximal respiration in RKO EC-R cells compared to RKO cells, indicating a substantial reduction in FAO in RKO EC-R cells (Figure 4, H and I). On the other hand, MOGAT3 knockout notably increased FAO in RKO EC-R cells relative to control cells (Figure 4, J and K). These data suggest that MOGAT3 mediated DAG accumulation by promoting DAG synthesis and inhibiting FAO in $BRAF^{V600E}$-mutant CRC cells.

MOGAT3-Induced DAG Accumulation Triggers MAPK Rebound

MAPK signaling rebound is recognized as an essential resistance mechanism in *BRAF* mutant tumor administration (23), so we tested whether combined MOGAT3 inhibitor with doublet therapy would inhibit phospho-ERK rebound more profoundly than anti-BRAF/EGFR treatment. Following doublet therapy, the BRAF and EGFR statuses were first assessed in resistant cells. Western blot analysis indicated that BRAF and EGFR signaling were suppressed in RKO EC-R, HT29 EC-R cells, and resistant PDX tumors post-treatment (Supplemental Figure 5E). Increased ERK and MEK phosphorylation were noted in RKO EC-R cells (Figure 5A), while MOGAT3 levels rose in resistant cells, predominantly localizing to the perinuclear region of the cytoplasm (Supplemental Figure 5, B and D). Genetic or pharmacological inhibition of MOGAT3, combined with anti-BRAF/EGFR therapy, markedly suppressed the upsurge in ERK and MEK phosphorylation (Figure 5, A and B). MOGAT3

knockdown significantly reduced DAG levels in RKO EC-R cells (Supplemental Figure 5A). We then investigated whether DAG accumulation, mediated by MOGAT3, leads to the reactivation of the MEK-ERK pathway. A critical role of DAG in signal transduction is its regulation of various cellular processes via the activation of protein kinase C (PKC), which occurs when DAG binds to the C1 domains of PKC, prompting its phosphorylation (24). As expected, we observed increased phosphorylated PKC (PKCα) in RKO EC-R cells (Figure 5C). To determine where DAG accumulates, we utilized the response of PKCα to DAG. We found that DAG levels were elevated in resistant cells and activated phospho-PKCα was localized to the cell membrane, co-localizing with E-cadherin (Figure 5D, Supplemental Figure 5, C and F). Previous studies reported that CRAF activation is a compensatory mechanism for BRAF inhibition (25), which could be phosphorylated by PKCα (26). Consistently, we observed the phosphorylated CRAF was elevated in RKO EC-R cells compared to RKO cells. Combined genetic or pharmacological inhibition of MOGAT3 with anti-BRAF/EGFR treatment effectively suppressed PKCα-CRAF signaling activation in RKO EC-R cells (Figure 5, C and E). To test if PKCα activation led to a MAPK rebound via CRAF activation, we knocked down PKCα and CRAF in RKO EC-R cells. The results indicated that PKCα knockdown diminished CRAF-mediated phosphorylation of ERK and MEK in RKO EC-R cells under doublet treatment (Figure 5F). And CRAF knockdown suppressed MEK-ERK signaling without affecting PKCα levels (Figure 5F). The activation of PKC through DAG or the PKC agonist PMA in RKO cells led to CRAF phosphorylation under

doublet treatment, triggering the MEK-ERK signaling cascade (Supplemental Figure 5G). This activation was abrogated by the PKC inhibitor PKC-IN-1 (Supplemental Figure 5G). Similarly, DAG plus doublet therapy activated phospho-PKCα/phospho-CRAF/phospho-MEK/phospho-ERK signaling in RKO cells (Supplemental Figure 5G). DAG-only treatment active phospho-PKCα/phospho-CRAF showed no exacerbating effect on phospho-MEK/phospho-ERK signaling compared to the control group (Figure 5G). On the contrary, the triplet therapy inhibited MOGAT3-mediated DAG accumulation and interrupted DAG-PKCα-CRAF signaling in resistant PDX tumors (Figure 5H). Treatment with Pf alone could inhibit phospho-PKCα/phospho-CRAF signaling but had no impact on phospho-MEK/phospho-ERK signaling, elucidating why Pf monotherapy is ineffective at halting the growth of drug-resistant tumors (Figure 5H and Figure 3I). In addition, overexpression of MOGAT3 in RKO cells caused an increase in DAG levels, which in turn promoted PKCα-CRAF signaling activation in CDX tumors, resulting in resistance to encorafenib/cetuximab treatment (Supplemental Figure 5H). These findings indicate that the accumulation of DAG mediated by MOGAT3 leads to PKCα-CRAF activation, thereby linking to the activation of MEK-ERK signaling.

Hypoxia-induced Resistance Upregulates MOGAT3, Enhancing DAG Accumulation and Tumor Resilience

Hypoxia and nutrient shortages in tumor mass accompanied by long-term treatment (27-29). Our GSEA results indicated that the HIF1A pathway was

significantly upregulated in resistant PDX tumors, and we observed that HIF1A protein expression was increased in resistant cells compared to parental cells (Figure 6，A and B, Supplemental Figure 6, A and B). To assess whether drug resistance status contributes to HIF1A elevation, we measured the HIF1A protein expression in RKO and RKO EC-R cells upon encorafenib/cetuximab treatment. Surprisingly, encorafenib/cetuximab treatment inhibited the protein level of HIF1A in the sensitive RKO cells but not in the resistant RKO EC-R cells, implying the inability to downregulate HIF1A was associated with drug resistance status (Figure 6C). Next, we examined whether HIF1A, a well-known transcription factor (30), regulated *MOGAT3* transcriptional expression. Inhibiting HIF1A by either siRNA or pharmacological inhibitor YC1 reduced the MOGAT3 protein expression level in the RKO EC-R cells (Figure 6D). Moreover, forced expression of HIF1A through hypoxic induction increased the protein expression level of MOGAT3 in the RKO cells (Figure 6E). The JASPAR predicted binding motif suggested HIF1A bound to the MOGAT3 promoter region, and the CHIP-PCR result revealed direct binding of HIF1A to the MOGAT3 promoter (Figure 6, F and G). Moreover, site-directed mutagenesis combined with luciferase assay indicated that binding sites 1 and 2 in the MOGAT3 promoter mainly mediated HIF1A-induced promoter activity (Figure 6H). We next asked whether HIF1A was regulated by DAG-mediated PKCα-CRAF signaling. In addition, we found that DAG-only treatment increases HIF1A protein expression in RKO cells and sensitive PDX tumors (Figure 6I, Supplemental Figure 6, C and D). Surprisingly, knockdown PKCα or CRAF suppressed HIF1A protein expression in RKO EC-R cells

(Figure 6J). Previous studies reported that eIF4E, a rate-limiting component of eukaryotic translation, could increase the translation of HIF1A protein (31, 32), and we observed that phosphorated eIF4E elevated in RKO EC-R cells compared to RKO cells (Figure 6K). On the other hand, inhibited PKCα-CRAF cascade suppressed eIF4E phosphorylation (Figure 6J) and directly inhibited phospho-eIF4E by tomivosertib reduced HIF1A protein expression in RKO EC-R cells (Figure 6L), canceled by the DAG supplement indicating PKCα-CRAF signaling promotes HIF1A elevation through eIF4E phosphorylation. HIF1A and eIF4E phosphorylation levels were increased in RKO EC-R cells under solo DAG treatment compared to the control group (Figure 6M). Then, to further investigate the causes behind the accumulation of MOGAT3 protein, we studied the impact of protein synthesis and degradation on MOGAT3 levels. We treated both sensitive and resistant cells with cycloheximide (CHX), a protein synthesis inhibitor, at various time points. Western blot analysis revealed that the rate of MOGAT3 protein degradation was similar in both sensitive and resistant cells (Supplemental Figure 6, E-H). Additionally, we treated sensitive and resistant cells with MG132, a proteasome inhibitor, and Eeyarestatin I (Eer I), an endoplasmic reticulum-associated degradation (ERAD) inhibitor. The results indicated that MOGAT3 protein levels rose following Eer I treatment, while MG132 treatment did not alter MOGAT3 levels in either cell type (Supplemental Figure 6, I and J). The increase of MOGAT3 protein levels following Eer I treatment was consistent in resistant and sensitive cell groups, suggesting that endoplasmic reticulum-associated degradation does not influence MOGAT3

accumulation on drug resistance (Supplemental Figure 6, I and J). These findings indicate that resistance-induced hypoxia promotes MOGAT3 transcriptional activation, and MOGAT3-mediated DAG accumulation reinforces resistance status through PKCα/CRAF/eIF4E/HIF1A cascade.

Fenofibrate overcomes the acquired resistance of *BRAF*^{V600E}-mutant mCRC to anti-BRAF/EGFR therapy

Acknowledging that the addition of a MOGAT3 inhibitor to anti-BRAF/EGFR therapy for the treatment of *BRAF*^{V600E}-mutant mCRC is unlikely to be clinically acceptable currently owing to concerns about toxicity in patients, we explored whether targeting DAG could lead to a more clinically appropriate regimen. Fenofibrate, an FDA-approved clinical drug, was designed to treat patients with hypertriglyceridemia, primary hypercholesterolemia, or mixed dyslipidemia (33) and can effectively reduce the levels of DAG. To evaluate the effectiveness of fenofibrate in resistant tumors, we treated resistant PDX tumors with vehicle (PBS), fenofibrate, encorafenib/cetuximab doublet, or fenofibrate plus encorafenib/cetuximab in vivo (Figure 7A and Supplemental Figure 7A). Triplet therapy, fenofibrate combined with encorafenib/cetuximab, significantly inhibited resistant PDX tumor growth, and doublet therapy or fenofibrate monotherapy showed modest compared to the vehicle group (Figure 7, A and C). As expected, the levels of DAG in resistant PDX tumors were dramatically decreased upon fenofibrate treatment (Figure 7B). In addition, histological analysis revealed that the triplet therapy markedly enhanced TUNEL

staining and decreased Ki67 expression in resistant PDX tumors (Figure 7, D and E). Then, we explored whether the treatment efficacy of triple therapy is dependent on MAPK signaling reduction. The PKCα-CRAF-MEK-ERK signaling was assessed in resistant PDX tumors. The western blot showed that the triplet treatment inhibited DAG-PKCα-CRAF signaling (Figure 7F). Consistent with the Pf-only treatment effects on resistant PDX tumors, fenofibrate-only treatment inhibited DAG-PKCα-CRAF signaling but showed no impact on MEK-ERK signaling (Figure 7F). Of note, the PKCα agonist (Phorbol 12-myristate 13-acetate, PMA) blocked the inhibition of tumor growth upon triple therapy, and PKCα or CRAF inhibitors (RAF-IN-1, PKC-IN-1) combined with encorafenib/cetuximab treatment suppressed resistant PDX tumor growth (Figure 7, G and H, Supplemental Figure 7C). Western blot results showed PKCα agonists reconnected the PKCα-CRAF signaling and inhibited treatment outcome in triple therapy (Figure 7I). Elevating DAG enhances HIF1A, implying that reducing DAG may modulate MOGAT3 (Figure 6I and Supplemental Figure 6C). To test whether fenofibrate influences MOGAT3, we measured its expression in resistant cells after fenofibrate treatment. Indeed, fenofibrate reduced MOGAT3 protein levels in RKO EC-R, HT29 EC-R, and resistant PDX tumors (Supplemental Figure 7B). Together, our data provide compelling evidence that fenofibrate overcomes the resistance of *BRAF*^{V600E}-mutant mCRC tumors to encorafenib/cetuximab treatment, depending on the MAPK signaling inhibition.

Discussion

Despite the latest approved encorafenib/cetuximab combination therapy benefits *BRAF*^{V600E}-mutant mCRC patients' survival, the duration time of this doublet therapy is far from satisfactory. Improving the durability of treatment effects of anti-BRAF/EGFR therapy in resistant *BRAF*^{V600E}-mutant mCRC patients is urgently needed. Ana Ruiz-Saenz *et al.* recently reported targeted inhibition of BRAF ± EGFR in *BRAF*^{V600E}-mutant mCRC systematically activated SRC parallel to MAPK signaling (7). *RNF43* mutations were found in partially BRAF ± EGFR treatment *BRAF*^{V600E} mutant mCRC patients, correlated with combination therapy efficiency (8). We discovered that SRC inhibitor solo or combined with BRAF ± EGFR treatment did not affect the tumor growth in our resistant models (data not shown). Moreover, whole exome sequencing analysis revealed no consistent mutations in resistant PDX tumors such as *RNF43*, ruling out genomic mutation as a cause of resistance. Our results provide an insight on how intratumoral lipid-DAG levels affect the response to anti-BRAF/EGFR therapy in *BRAF*^{V600E}-mutant mCRC by activating PKCα-CRAF-MEK-ERK signaling, leading to acquired resistance. Our valid evidence showed that MOGAT3-mediated DAG accumulation triggers a rebound in the MAPK pathway, conferring resistance to encorafenib/cetuximab therapy. Noticeably, resistance-induced hypoxia leads to increased *MOGAT3* transcription, with MOGAT3-mediated DAG accumulation strengthening resistance via elevated PKCα/CRAF/eIF4E/HIF1A signaling. In contrast, inhibiting MOGAT3 decreases intratumoral DAG and dampens PKCα-CRAF-MEK-ERK signaling, enhancing the effectiveness of

encorafenib/cetuximab doublet therapy in resistant *BRAF*^{V600E}-mutant mCRC. Interestingly, fenofibrate, a clinically actionable drug, overcomes the acquired resistance to encorafenib/cetuximab therapy in *BRAF*^{V600E}-mutant mCRC in vivo through DAG reduction and subsequent inhibition of PKCα-CRAF-MEK-ERK signaling. Our study uncovered a lipid-mediated resistance mechanism in *BRAF*^{V600E}-mutant mCRC and suggested a viable clinical approach to counter resistance to anti-BRAF/EGFR therapy.

Diacylglycerols (DAGs) are central to multiple metabolic processes and mediated signaling transduction (34). Dysregulation of DAG metabolism is thought to affect cellular signaling adversely and is involved in developing various disease states, such as insulin resistance (35). Most notably, protein kinase C (PKC) senses diacylglycerol (DAG) generated in the different cellular compartments in various physiological processes (36). Recent studies reported that diacylglycerol kinase α (DGKα) facilitated phosphatidic acid synthesis by consuming DAG to negatively regulate the lipogenic transcription factor SREBP-1 in CRC tumor cells, implying the signal transduction function of DAG in controlling tumor growth (37). We report that the level of intratumoral DAG determines the response of anti-BRAF/EGFR therapy in *BRAF*^{V600E}-mutant mCRC, enriched knowledge in the DAG regulation of tumor targeted therapy. DAG accumulation induced by resistance is mainly concentrated in tumor cells, and we evidenced that DAG-mediated phosphorylated PKCα/CRAF activation results in combination therapy treatment failure. The increase or decrease of DAG in *BRAF*^{V600E}-mutant tumors does not independently affect tumor growth; it

is related to therapeutic interventions. Further research indicated that DAG modulates phospho-PKCα/phospho-CRAF signaling without impacting phospho-MEK/phospho-ERK pathways. The proliferation of resistant $BRAF^{V600E}$-mutant tumors is governed by BRAF/CRAF-mediated MEK/ERK signaling. In $BRAF^{V600E}$-mutant tumors with resistance, targeting either CRAF or BRAF alone does not disrupt MEK/ERK signaling, which is why neither MOGAT3 inhibition (with Pf-06471553) nor DAG reduction (through fenofibrate) is sufficient to hinder the growth of resistant tumors. On the other hand, MOGAT3-mediated DAG accumulation elevated the phosphorylated expression of eIF4E by PKCα/CRAF activation and then translational promoted HIF1A protein expression, reinforcing hypoxia and acquired resistance statutes (32, 38). Short-term doublet therapy showed no effect on HIF1A. DAG plus doublet increased HIF1A protein expression, suggesting acquired resistance-induced hypoxia, and the resistant status in $BRAF^{V600E}$-mutant mCRC is bilateral enhanced under DAG accumulation. Moreover, our data showed that DAG enhances HIF1A signaling in $BRAF^{V600E}$-mutant colorectal cancer (CRC). HIF1A, a critical transcription factor for cancer cell survival, orchestrates the expression of genes related to metabolism and survival, enabling adaptation to adverse microenvironments (39). The involvement of HIF1A in glucose metabolism, particularly in the context of the Warburg effect, has been the subject of extensive research over the last two decades (40). Upon activation, HIF1A stimulates the uptake of fatty acids and enhances lipid storage (41). Furthermore, HIF1A inhibits fatty acid oxidation by downregulating PGC-1α, CPT1A, and acyl-CoA dehydrogenases, and it also hampers

lipolysis by repressing ATGL(42). In line with these findings, we observed a decrease in fatty acid oxidation (FAO) and CPT1A expression in resistant cells with elevated DAG levels compared to sensitive cells. This may account for the observed inhibition of FAO in resistant *BRAF*^{V600E}-mutant CRC cells with high DAG levels. These results suggest an intimate association between the lipid metabolite accumulation in modulating the tumor resistance of mCRC with *BRAF*^{V600E}-mutant, which provided a therapeutic insight into overcoming drug resistance via metabolic rewiring.

Monoacylglycerol acyltransferase 3 (MOGAT3) is primarily expressed in the gastrointestinal tract (16). As an integral membrane enzyme, MOGAT3 catalyzes the acylation of monoacylglycerol (MAG) and diacylglycerol (DAG), promoting DAG synthesis (18). Previous evidence has suggested that MOGAT3 has MOGAT and DGAT activity (36), yet its role and impact on disease progression remain unclear. We found that hypoxia induced by acquired resistance status upregulates MOGAT3 transcription, leading to DAG accumulation and affecting the efficacy of doublet treatment efficiency. Moreover, upregulated MOGAT3 enhances DAG synthesis while simultaneously decreasing its breakdown, promoting DAG accumulation in a bidirectional manner.

Recent studies have illustrated the mechanism of treatment failure of BRAF ± EGFR in *BRAF*^{V600E} mutant mCRC but have not resolved the resistance issue in our models. The resistance of *BRAF*^{V600E}-mutant tumors to anti-BRAF/EGFR therapies is primarily attributed to the rebound activation of MAPK signaling (23). Indeed, our results showed that MOGAT3-mediated DAG accumulation drives

resistance through PKCα-CRAF mediated MAPK re-activation. Clinical studies have proved that the synergistic treatment of MEK inhibitors has no impact on prolonging the duration of patients' anti-BRAF/EGFR therapies (6). Developing a clinical treatment to overcome drug resistance is time-consuming and labor-intensive. Our data demonstrated that MOGAT3/DAG signaling drives acquired resistance in *BRAF*^{V600E}-mutant mCRC, and targeting DAG equivalent to MOGAT3 inhibition overcomes the resistance. Impressively, fenofibrate plus encorafenib/cetuximab ideally inhibits resistant tumor growth with levels of intratumorally DAG reduction. In our model, the levels of DAG in *BRAF*^{V600E}-mutant CRC tumors determine the efficiency of doublet therapy. Lower DAG by MOGAT3 inhibition re-response of the resistant cells to doublet therapy. On the other hand, the FAO was inhibited in resistant cells compared to sensitive cells, which might contribute to high levels of DAG. Lower DAG by fenofibrate, manifested as fenofibrate, re-sensitive the effects of doublet therapy to resistant *BRAF*^{V600E}-mutant mCRC tumors. These effects of fenofibrate indicate that DAG-mediated downstream activation was disrupted by fenofibrate. Further, our results illustrated that DAG accumulation also increases the expression of MOGAT3 in a transcriptional manner to strengthen drug resistance. Lowering DAG by fenofibrate could reduce DAG levels and inhibit MOGAT3 expression. This triplet therapy has shown clinical promise in overcoming resistance in *BRAF*^{V600E}-mutant mCRC. Moreover, we noted that elevated blood lipids correlate with resistance to encorafenib/cetuximab combination therapy in PDX models. During the follow-up of clinical drug treatment, we observed an increase in serum

lipids. This increase seems to be related to the ineffectiveness of the encorafenib/cetuximab combination therapy, and further investigation is warranted.

In conclusion, our results demonstrate that MOGAT3-mediated DAG accumulation has a dominant role in mediating the acquired resistance of $BRAF^{V600E}$-mutant mCRC to anti-BRAF/EGFR therapy. We evidenced that resistance-induced hypoxia promotes MOGAT3-mediated DAG accumulation and drives PKCα-CRAF-MEK activation; in parallel, accumulated DAG reinforces resistant status by PKCα/CRAF/eIF4E/HIF1A signaling activation. We propose a clinically viable enhancement strategy involving triplet therapy with fenofibrate combined with encorafenib/cetuximab to improve treatment efficiency in $BRAF^{V600E}$-mutant mCRC.

Methods

Sex as a biological variable. Our study exclusively examined female mice. It is unknown whether the findings would be similar for male mice, although we would not expect significant differences in the results.

Patient samples. The established PDX (derived from the primary tumor) originated from a 68-year-old male patient who presented with primary transverse colon cancer with liver metastasis and underwent laparoscopic resection of the left colectomy procedure. Molecular pathology testing found that the patient had *RAS* wild type, $BRAF^{V600E}$, *TP53* mutation, and *MSS* status. Before surgery, the patient had not received BRAF/EGFR inhibitor therapy. The tumors in situ were directly snap-frozen or fixed in formalin and embedded in paraffin for further use.

Patient-Derived Xenograft (PDX). All procedures involving animals were carried out under the guidelines of the Institutional Animal Care and Use Committee. Fresh $BRAF^{V600E}$-mutant mCRC tissue was collected in RPMI640 medium with anti-tissue biotics, rinsed in PBS, and transplanted subcutaneously in the groin of 4-week-old female BALB/C nude mice. Sedation and analgesia were performed using ketamine, medetomidine, and buprenorphine. Upon reaching generation 3, tumor fragments were transplanted into nude mice. The tumor size reached 150 mm^3 and was defined as the baseline as a control time point for the efficacy of subsequent dosing(43). Mice were randomly assigned to a cohort, and drugs or vehicles were blindly administered

daily by oral gavage and intraperitoneal injection twice a week. Encorafenib was administered orally at 20 mg/kg daily, and cetuximab intraperitoneal injection at 20 mg/kg twice weekly (19). Tumor size was measured by digital calipers every 3 days. After the treatment of BRAF/EGFR inhibitors, the subcutaneous tumors of mice continued to decrease in volume, defined as the BRAF/EGFR inhibitors' sensitive time. An initial reduction in tumor size in the experimental group followed by a re-growth of more than 150 mm^3 represented a successful establishment of a PDX model that is resistant to BRAF/EGFR inhibitors, which was defined as the BRAF/EGFR inhibitors resistant time. The sensitive and resistant tissues were reinoculated on nude mice again, respectively, using the exact dosage as above, to validate PDX tumor response to BRAF/EGFR inhibitors. In the follow-up PDX experiments, we used sensitive or resistant tissues for PDX modeling. Mice were sacrificed at 28 days following the start of treatment or when tumors reached a volume of 1500 mm^3. The investigators were blinded for the evaluation of the results. Once the PDXs were obtained, blood samples were collected from the eyelids of nude mice, after which mice were sacrificed to obtain tumor tissues.

Cell lines and drug treatment. Two colorectal cancer (CRC) cell lines, HT29 and RKO cells with a $BRAF^{V600E}$ mutation were obtained from the American Type Culture Collection (ATCC, Manassas, Virginia, USA). The human embryonic kidney cell line HEK-293T was purchased from the Cell Bank of the Shanghai Academy of Chinese Sciences. The mutational status of these cell lines utilized in this research can be

accessed from the Cancer Cell Line Encyclopedia (CCLE) database and a prior study (44). All cell lines were cultured in Dulbecco's modified essential medium (DMEM) or McCoy's 5A medium containing 100 μg/mL streptomycin, 100 μ/mL penicillin, and 10% fetal bovine serum (FBS, Gibco, NY, USA). The cells were incubated at 37 °C in a 5% humidified CO2 atmosphere. All the cell lines utilized in the study were negative for mycoplasma contamination (Cat. No. LT07-318; Lonza). DAG (Sigma, 24529-88-2) was dissolved in fresh dimethyl sulfoxide (DMSO) for a stock solution at 50 mM (or 50 mg/ml for the in vivo study). Similarly, TAG (Sigma, 1716-07-0) was dissolved in fresh DMSO to 50 mM. A working solution was added with pre-set DAG and TAG concentrations by mixing common serum-free medium proportionately. Encorafenib (MCE, HY-15605), Cetuximab (MCE, HY-P9905), and Pf-06471553 (MCE, HY-108339) were treated the cells after dissolving the dilution according to the instructions.

Cell Line Derived Xenograft (CDX). Approximately 2×10^6 RKO EC-R, RKO EC-R-MOGAT3^{KO} cells were subcutaneously injected into the right hind limbs of BALB/C nude mice. Treatment began 1 week following the injection. The mice were randomized into three groups (n = 6 per group) and intraperitoneally injected with vehicle (PBS), cetuximab (20 mg/kg/intraperitoneally twice a week) + encorafenib oral administration (20 mg/kg/day) two together or combined with DAG intraperitoneally injected (50mg/kg/day). Tumor growth was recorded every 3 days from 1 week after inoculation by measurement of two perpendicular diameters using

627 the formula $4\pi/3 \times (\text{width}/2)^2 \times (\text{length}/2)$. Mice were sacrificed 4 weeks after
628 inoculation. The masses of tumors (mg) derived from treatments were compared. In
629 the MOGAT3-overexpression model, 2×10^6 cells (RKO NC, RKO OE-MOGAT3)
630 were in a mixture of PBS in a volume of 100 μL, which were then injected into the
631 subserous layer of the middle of nude mice cecum. After four weeks, all mice were
632 sacrificed.
633
634 *Biochemical indicators quantification.* The levels of diglycerides in PDX tumor
635 lysates were measured using the Diacylglycerol Assay Kit (Cloud-Clone Corp,
636 CEC038Ge) following the manufacturer's instructions. AST, ALT, CR, and BUN
637 levels in rat serum were measured accordingly using the Assay Kit (ALT01, AST01,
638 URE01, G034) following the manufacturer's instructions and were detected in
639 Automatic Biochemical Analyzer LWC400.
640
641 *Cell viability assay.* Cell viability was assessed using the Cell-Counting Kit-8 (CCK8)
642 from Dojindo Molecular Technologies, according to the manufacturer's instructions.
643 The absorbance was measured at 450 nm using a microplate reader. The experiments
644 were conducted in triplicate.
645
646 *Diacylglycerol and Triglyceride Assay.* Intracellular and tissue diacylglycerol (DAG)
647 were determined with a DAG ELISA Kit (Cloud-clone corp, CEC038Ge), and
648 triglyceride (TAG) was detected by TAG content enzymatic assay kit (Applygen,

E1013-50) according to the manufacturer's instructions.

RNA sequencing analysis and whole exome sequencing. Total RNA of indicated tumor tissues from baseline, sensitive, and resistant periods were extracted using the TRIzol reagent (Invitrogen, CA, USA) according to the manufacturer's protocol. RNA purity, quantification, and integrity were evaluated. Then, the libraries were constructed using VAHTS Universal V6 RNA-seq Library Prep Kit according to the manufacturer's instructions. Subsequently, paired-end sequencing on an Illumina Novaseq™ 6000 (LC-Biotechnology CO., Ltd., Hangzhou, China) was performed following the vendor's recommended protocol. The total DNA was extracted using QIAamp DNA FFPE Tissue (QIAGEN). Then, the DNA, which was fragmented using the Covaris M220 Focused-ultrasonicator (Covaris), was subjected to sequencing library construction. Exome capture was performed using SureSelect Human All Exon V6 Kit (Agilent Technologies) following the vendor's recommended protocol. The sequencing was performed using the Illumina Novaseq™ 6000 (LC-Bio Technology CO., Ltd., Hangzhou, China) with 150-bp paired-end sequencing mode. The transcriptome sequencing, whole exome sequencing, and its analysis were conducted by Lianchuan Biotech Co., Ltd. (Hangzhou, China).

Lipidomic analysis. Indicated RKO, RKO EC-R, RKO EC-R MOGAT3^{KO} cells were collected for lipid extraction, which were then analyzed by Thermo Scientifific Dionex UltiMate 3000 HPLC system (Thermo Scientifific, Sunnyvale, CA, USA)

equipped with a Q Exactive hybrid quadrupole-Orbitrap mass spectrometer (Thermo Scientifific, Waltham, USA). For the UHPLC–MS/MS analysis, chromatographic lipids were separated using the UHPLC-Q Exactive HF-X Vanquish Horizon system (Thermo, USA) by Majorbio (Shanghai, China). After UPLC-MS/MS analyses, the raw data were imported into LipidSearch (Thermo, CA) for peak detection, alignment, and identification. MS/MS fragments identified the lipids. The data were analyzed through the free online platform of the central cloud platform (cloud.majorbio.com).

RNA interference (RNAi) and Lentiviral transfection. Small interfering RNAs (siRNAs) targeting MOGAT3 were synthesized from Gene Pharma (Shanghai, China) and transfected into the RKO EC-R and HT29 EC-R cell lines with Lipofectamine RNAiMAX (Invitrogen, CA, USA). Stable MOGAT3 overexpression RKO cells were established using MOGAT3 overexpression plasmid (purchased from Qingke Co. Ltd., Nanjing, China). According to the manufacturer's instructions, lentivirus production and infection were performed with Lipofectamine 3000 (Invitrogen, CA, USA). CRISPR-Cas9 editing system was employed to create MOGAT3-KO cells in RKO EC-R and HT29 EC-R cells based on the manufacturer’s protocol. Additionally, we generated the PCDH-CMV-MCS-EF1-GFP-Puro vector (Tsingke).

RNA isolation and quantitative RT-PCR (qRT-PCR). Total RNA was extracted from cells using the Trizol reagent (Invitrogen). Subsequently, cDNA was synthesized using the cDNA reverse transcriptase kit (Takara). SYBR Green-based quantitative

real-time PCR (RT-qPCR) was carried out using the LightCycler 480 real-time PCR system (Roche, Mannheim). The primer sequences are listed in Table S1.

Antibodies and Western blotting. After being treated with RIPA buffer containing protease inhibitors and phosphorylase inhibitors, protein concentration was determined using a BCA Protein Assay Kit (Beyotime), then samples were supplemented with DTT (Sigma), sonicated, and boiled for 10 minutes. Equal amounts of protein were loaded onto 4%-12% SDS-PAGE and then transferred to PVDF membranes (Millipore, Schwalbach, Germany). The membranes were incubated with the appropriate antibodies. All antibodies were used at the recommended dilution (Table S2).

Oil red O staining. Frozen cancer tissues were embedded in the OCT compound (Sakura, Tokyo, Japan) and cut into 10μm sections. The sections were washed several times with distilled water, followed by pre-incubation in 60% isopropanol before being finally stained with a filtered Oil Red O working solution (consisting of 60% Oil Red O stock solution (BA-4081, Baso, Zhuhai, China) and 40% deionized water. After a series of washing steps in 60% isopropanol, the nuclei were counterstained with hematoxylin and differentiated in 1% hydrochloric acid in alcohol. Finally, the slides were washed several times with distilled water and sealed with glycerin gelatin. Representative images were captured using an inverted microscope (Olympus, Tokyo, Japan).

Immunofluorescence (IF). 5,000 cells were plated in each confocal dish. Media were aspirated, and cells were fixed with 2% paraformaldehyde in PBS for 10 minutes. The confocal dish was washed twice with 0.1% Triton X-100 in PBS. A blocking solution (2% BSA) was added for 1h, followed by primary antibodies (Supplemental Table 2) diluted in the blocking solution at 1:500 and incubated at 4°C overnight. The next day, confocal dishes were washed twice with PBS. Secondary antibodies were FITC-conjugated donkey anti-rabbit IgG, Alexa Fluor 647 conjugated donkey anti-rabbit IgG, and Alexa Fluor 488-conjugated goat anti-mouse IgG1 (Invitrogen, Thermo Fisher Scientific). Cells were mounted with a fluorescence mounting medium containing DAPI (ab104135, abcam). IF results were imaged using the Zeiss LSM 800 Confocal. Data were processed using ZEISS ZEN software.

Nile red staining. The tumor tissue slides were seeded on cover glasses and fixed using 4% paraformaldehyde (PFA) for 20 minutes at room temperature. Subsequently, Nile red (HY-D0718, MCE, USA) was added at a 1:2000 dilution in phosphate-buffered saline (PBS) for 10 minutes. Afterward, the slides were counterstained with DAPI (HY-D0814, MCE, USA) at a concentration of 1μg/ml in PBS for 5 minutes at room temperature before imaging. The slides were visualized using a fluorescence microscope (Olympus, Tokyo, Japan).

BODIPY 493/503 staining. Cells were fixed in 4% PFA for 20 min at RT and

incubated with BODIPY 493/503 (D3299, Thermo Fisher, USA) at 1:2000 and DAPI (HY-D0814, MCE, USA) in PBS for 15 min at RT. Finally, the cells were visualized with a fluorescence microscope (Olympus, Tokyo, Japan).

Immunohistochemistry (IHC). Immunohistochemistry (IHC) was performed as previously described (45). Semi-quantitative scoring was used to analyze the results of IHC. According to the dyeing intensity, the grading was as follows: non-dyeing scored 0, light yellow scored 1, brown, yellow scored 2, and brown scored 3. The mean values of five visual fields (×400) were taken to calculate the percentage of positive tumor cells in all visual fields. The percentage of positive tumor cells in the visual field < 1% scored 0, 1–25% scored 1, 25–75% scored 2, and 75–100% scored 3. The final score was the sum of the dyeing intensity and positive cell scores. Antibodies used here are listed in Table S2. All these antibodies were used at the recommended dilution according to the manufacturer's instructions.

TUNEL assay. In situ, cell death paraffin-embedded specimens were tested using a cell death detection kit (11684795910, Roche, USA), according to the manufacturer's instructions. Representative TUNEL images were captured using an inverted microscope (Olympus, Tokyo, Japan).

Apoptosis analysis and tumor cell sorting. The number of apoptotic cells was determined using an Annexin V-FITC apoptosis kit (BD Biosciences, NJ, USA),

following the manufacturer's instructions. Cells from different groups were harvested with 0.25% trypsin and washed with PBS. After centrifugation, the cells were resuspended in 100μl of buffer and stained with 3μl of Annexin V and 5μl of propidium iodide (PI). The mixture was incubated in the dark at 4°C for 15 min. The cells were sorted using a FACS Calibur flow cytometer (BD Biosciences, USA), and 10,000 cells per sample were counted during the assay. The results were analyzed using Cell Quest software (BD Biosciences, USA). The experiments were repeated three times. Briefly, tumors were digested using DNase I (D5025; Sigma-Aldrich) and Collagenase Type II (07419; STEMCELL), followed by treatment with ACK lysis buffer (A10492-01; Gibco). Cells were blocked for 15 min on ice with Human TruStain FcX Fc Receptor Blocking Solution (422301; Biolegend). For flow-cytometric analysis of epithelial cells and immune cells, cells were stained for 30 min on ice with CD45-PE (1:100; BioLegend), CD326 (EpCAM)-APC-cy7 (1:100 BioLegend) and Zombie Violet™ dye (1:200, BioLegend). Cells were resuspended in PBS and analyzed on a CytoFLEX SRT Cell Sorter. Flow gating strategies were kept consistent between samples to enable comparison across cohorts.

Chromatin immunoprecipitation assay and Double luciferase reporter gene experiment. Chip was carried out via chip kit (P2080S, Beyotime, Jiangsu, China) according to the manufacturer's recommended protocol. Antibody and primer sequences are listed in the Tables. S1-2. The cells were plated in 24-well plates at a density of 3×10^4 cells per well and then transfected with 0.5 μg of the promoter-

781 luciferase plasmid. Meanwhile, 0.5 μg of pRL-CMV (Renilla luciferase) was also
782 transfected to normalize the transfection efficiency. Luciferase activity was measured
783 using a Dual-Luciferase Assay kit (Promega) after 48h transfection and a full-
784 wavelength microplate reader (Varioskan Flash, Thermo Scientific) following the
785 manufacturer's guidelines.
786
787 *Seahorse Analysis.* The Seahorse XFe 96 Extracellular Flux Bioanalyzer from Agilent
788 was utilized to measure the oxygen consumption rate (OCR) according to the
789 manufacturer's protocol. After plating the cells in a 96-well plate for 24 hours, cells
790 were placed in fresh DMEM medium comprising 10mM glucose, 2mM L-glutamine,
791 and 1mM sodium pyruvate and incubated for 1 hour. To each well, three metabolic
792 inhibitors were added sequentially, namely oligomycin (Oligo, 1μM), followed by
793 carbonyl cyanide 4-trifluoromethoxy-phenylhydrazone (FCCP) (2μM), and then
794 rotenone (Rot, 2μM).
795
796 *FAO assay.* An FAO assay was conducted following the protocol provided by Abcam
797 (ab222944). In brief, approximately 6×10^4 cells were seeded into 96-well plates, and
798 positive controls were treated with 2.5μM carbonyl cyanide 4-(trifluoromethoxy)
799 phenylhydrazone (FCCP), while negative controls were treated with 40μM Etomoxir.
800 Rates of FAO were calculated by determining the slopes (m) from the linear portion
801 of each profile and using the formula.
802

Statistics. Data were presented as the mean ± standard error mean (SEM) of three independent experiments. Comparisons were analyzed using 2-tailed unpaired t-test or 1-way ANOVA with Tukey's multiple-comparison test or 2-way ANOVA with Tukey's multiple-comparison test. Statistical analyses were conducted using GraphPad Prism version 9.0. or SPSS Statistics software. *P < 0.05, **P < 0.01, ***P < 0.001.

Study approval. The Medical Ethical Board of the Sir Run Run Shaw Hospital, School of Medicine, Zhejiang University has approved the collection and use of human tumor tissue for the PDX model (study number 20220209-93).All animal procedures were conducted strictly with institutional guidelines and were approved by the Medical Ethical Board of the Sir Run Run Shaw Hospital, School of Medicine, Zhejiang University (SRRSH202202112).

Data availability. Raw data are accessible in NODE (https://www.biosino.org/node) with the accession number OEP00005624 or through the URL: https://www.biosino.org/node/project/detail/OEP00005624. All data values reported in this work are available in the Supporting Data Values file.

Authors' Contributions

Z.S. contributed to conceptualization and methodology. J.W., H.W., W.Z., X.L., H.W., Q.M., J.C., and X.Y. performed experiments. J.W., H.W., W.Z., and Z.S. performed

data, bioinformatic and statistical analyses. Z.S., W.Z., and Y.J. provided reagents and resources. J.W., H.W., W.Z., Y.L, D.C., and Z.S. contributed to paper drafting and editing. Z.S. provided guidance and supervision. Z.S. and W.Z. H.W. provided funding support. All authors reviewed the manuscript.

Acknowledgments

This research was funded by the National Natural Science Foundation of China (No.82273265, No.82373163, No.82403563), Zhejiang Provincial Natural Science Foundation of China (No. LY23H160022, LQ24H160020), and the Zhejiang Province Research and Development Program of "Lingyan" (No.2023C03065).

Figure legends

Figure1. Encorafenib and cetuximab resistant *BRAF*^{V600E}-mutant mCRC tumors exhibited abnormal lipid metabolism activity

A. Patient-derived *BRAF*^{V600E}-mutant mCRC samples: Computed tomography picture shows primary tumor location (left) and H&E morphology of original primary and PDX tumor mass (right).

B. Mean tumor volumes (±SEM) of *BRAF*^{V600E}-mutant mCRC PDXs treated with encorafenib and cetuximab relative to baseline (T0) (n=6).

C. Bubble plot showed KEGG pathways of up-regulated genes enriched in resistant PDX tumors versus sensitive PDX tumors based on RNA-seq data (n=3).

D. Heatmap showed metabolic pathways genes related to Fig1C (n=3).

E. Bar chart presenting a classification of metabolic pathways genes related to Fig.1D.

F. Gene set enrichment analysis (GSEA) of resistant tumors versus sensitive tumors (n=3) showed enhanced lipid metabolic process. Normalized enrichment score (NES) and nominal p-value (*p*) were provided according to GSEA.

G. Lipid droplet content of tumors was assessed by Nile red staining over three periods. The representative images were shown from three independent experiments. Scale bar, 20μm.

H. RKO, RKO EC-R, and HT29, HT29 EC-R cells were stained with BODIPY 493/503(green). The representative images were shown from three independent experiments. Scale bar, 10μm.

Figure 2. DAG accumulation drives the acquired resistance of *BRAF*^{V600E}-mutant mCRC to BRAF/EGFR inhibitors treatment

A. Bubble plots showed KEEG pathways of upregulated metabolites enriched in RKO EC-R versus RKO cells based on lipidomic (n=6).

B. DAG content in PDX tumors (n=6) and DAG content in tumor epithelial cells (n=3).

C-F. Xenograft tumor size in nude mice inoculated with encorafenib-cetuximab-sensitive *BRAF* ^{V600E}-mutant mCRC tumor tissues (n=6). PDXs were treated with vehicle (PBS), encorafenib-cetuximab, and encorafenib-cetuximab combined with intraperitoneal injection with DAG or DAG alone (C). Tumor weight (D), tumor growth (E) and intratumoral DAG level (F).

G-H. Representative images of H&E, Ki67, oil red staining, and TUNEL staining are related to Figure 2C (G). Ki67 and TUNEL quantitation (H) (n=3).

The data were presented as the mean ± SEM of three independent experiments, ns, no significance; *$p < 0.05$, **$p < 0.01$, and ***$p < 0.001$. (2-tailed unpaired t test in B; 1-way ANOVA with Tukey's multiple-comparison test in D, F and H; 2-way ANOVA with Tukey's multiple-comparison test in E).

Figure 3. MOGAT3 mediated DAG elevation determines anti-BRAF/EGFR treatment failure in *BRAF*^{V600E}-mutant mCRC tumors

A. Representative IHC images of MOGAT3 in baseline, sensitive, and resistant tumor tissues. Scale bar, 100μm. Western blot showed protein expression of MOGAT3 in RKO, RKO EC-R, and HT29, HT29 EC-R cells. Representative blots were shown.

B. The MOGAT3-knockout RKO EC-R and HT29 EC-R, along with RKO EC-R-CTRL and HT29 EC-R-CTRL cell lines, were exposed to encorafenib (2μM)/cetuximab (4μM) for 96h, upper panel of western blot showed protein expression of MOGAT3. Relative OD value was assessed to determine cell viability by the CCK-8 assay (n=3).

C-E. Xenograft tumor size in nude mice inoculated with RKO EC-R cells (CTRL), RKO EC-R cells MOGAT3^{KO} cells, and treated with encorafenib-cetuximab both or in combination with intraperitoneal injection with DAG (C). Tumor weight (C), Tumor DAG level (D), and tumor growth (E) in nude mice (n=6).

F-H. Xenograft tumor size in nude mice inoculated with RKO cells (Nc)、RKO Oe-MOGAT3 cells and treated with encorafenib-cetuximab (F). Xenograft tumor weight (F), DAG level in tumor tissues (G), and tumor growth (H) (n=6).

I-K. Xenograft tumor size in nude mice inoculated with encorafenib-cetuximab-resistant *BRAF* ^{V600E}-mutant mCRC tumor tissues. PDXs corresponding respectively treated with vehicle (PBS), encorafenib (20mg/kg)-cetuximab (20mg/kg), MOGAT3 inhibitors PF-06471553 (50mg/kg) alone or in combination with encorafenib-cetuximab (I). Xenograft tumor weight (I), DAG level in tumor tissues (J), and growth (K) in nude mice (n=6).

The data were presented as the mean ± SEM of three independent experiments, ns, no significance; *$p < 0.05$, **$p < 0.01$, and ***$p < 0.001$. (2-tailed unpaired t test in F and G; 1-way ANOVA with Tukey's multiple-comparison test in C, D, I and J; 2-way ANOVA with Tukey's multiple-comparison test in B, E, H and K).

Figure 4. Highly expressed MOGAT3 promotes lipid synthesis and inhibits lipid-OXPHOS, resulting in DAG accumulation.

A. Western blot showed the protein expression levels of LPIN1 and MOGAT3 in RKO and RKO EC-R cells. Representative blots were shown.

B. Schematic diagram of the main DAG synthesis pathway.

C. DAG level in RKO EC-R MOGAT3^{KO} CDX (n=6).

D-E. Oxygen consumption rate (OCR) in RKO and RKO EC-R cells (D). Oligo, oligomycin; FCCP, carbonyl cyanide 4-trifluoromethoxy-phenylhydrazone; Rot, rotenone. OXPHOS-related indicators were quantified (E) (n=4).

F-G. Oxygen consumption rate (OCR) in RKO EC-R and RKO EC-R MOGAT3^{KO} cells (F). Oligo, oligomycin; FCCP, carbonyl cyanide 4-trifluoromethoxy-phenylhydrazone; Rot, rotenone. And OXPHOS-related indicators were quantified (G) (n=8).

H-K. FAO assay of RKO, RKO EC-R cells (H), and RKO EC-R MOGAT3^{KO} cells (J). Cells treated with FCCP were used as the positive control, and cells treated with Eto were used as the negative control. Eto, Etomoxir. Graphs at the right panel showed relative FAO rates (I) (K) (n=3).

The data were presented as the mean ± SEM of three independent experiments, ns, no significance; *$p < 0.05$, **$p < 0.01$, and ***$p < 0.001$. (2-tailed unpaired t test in C, E, G, I and K; 2-way ANOVA with Tukey's multiple-comparison test in H and J).

Figure 5. MOGAT3 reactivates MAPK through DAG mediated PKCα/CRAF axis

A. RKO EC-R cells transfected with siRNA-NC, siRNA-MOGAT3-1$^{\#}$ or siRNA-MOGAT3-2$^{\#}$ treated with encorafenib (2μM)-cetuximab (4μM) for 72h. Western blot assessed MOGAT3 and MEK/ERK signaling. Representative blots were shown.

B. Immunoblot analysis of MEK/ERK signaling in RKO EC-R cells treated with encorafenib (2μM)-cetuximab (4μM), PF-06471553 (10μM) alone or a combination of both PF for 48 hours.

C. RKO EC-R cells transfected with siRNA-NC, siRNA-MOGAT3-1$^{\#}$ or siRNA-MOGAT3-2$^{\#}$ treated with encorafenib (2μM)-cetuximab (4μM) for 72h.Western blot detected MOGAT3 and PKCα/CRAF signaling.

D. Immunofluorescence of phospho-PKCα signaling in HT29 and HT29 EC-R cells. Representative images were shown. Scale bar, 10μm.

E. Immunoblot analysis of PKCα/CRAF signaling in RKO EC-R cells treated with encorafenib (2μM)-cetuximab (4μM), Pf-06471553 (10μM) alone or a combination of both Pf for 48 hours.

F. Western blot detected PKCα/CRAF and MEK/ERK signaling in RKO EC-R cells treated with siRNA-PKCα, siRNA-CRAF, or a combination of both for 48 hours.

G. Immunoblot analyzed of PKCα/CRAF and MEK/ERK signaling in RKO cells treated with encorafenib (0.25μM)-cetuximab (0.5μM), DAG (10μM) or a combination of both DAG (10μM) for 48 hours.

H. Western bolts detected the intracellular signal change in encorafenib/cetuximab-resistant PDXs from Figure 3I. The tumor tissues were harvested for western blotting to detect the indicated signaling proteins. A representative blot was shown from three independent experiments.

Figure 6. Accumulated DAG enhances *MOGAT3* transcription expression through PKCα/CRAF/eIF4E/HIF1A signaling activation

A. Gene set enrichment analysis (GSEA) of resistant tumors versus sensitive tumors (n=3) showed enhanced HIF1A signaling pathway. Normalized enrichment score (NES) and nominal *p*-value (*p*) were provided according to GSEA.

B. Immunoblot analysis of MOGAT3 and HIF1A in RKO and RKO EC-R cells.

C. Immunoblot analysis of HIF1A and MOGAT3 in RKO, RKO EC-R cells treated with encorafenib-cetuximab for 48 hours.

D. Immunoblot analysis of HIF1A and MOGAT3 in RKO EC-R cells after siRNA-HIF1A knockdown for 72 hours (left) or treated with the indicated concentrations of YC-1(1μM) for 24 hours (right).

E. Immunoblot analysis of HIF1A and MOGAT3 in RKO cells after hypoxia for 0, 4, 8, and 12 hours.

F. Illustration of HIF1A site in MOGAT3 promoter and the predicted HIF1A site in MOGAT3 promoter. The HIF1A motif from the ACGTGC promoter was predicted by the website JASPAR 2022.

G. Chip-PCR confirms that HIF1A can directly transcriptionally regulate *MOGAT3* (left), RT-qPCR of chip-PCR (right) (n=3).

H. Luciferase reporter assay shows that HIF1A overexpression significantly activated the promoter activity of MOGAT3 (n=3).

I. Immunoblot analysis of MOGAT3, HIF1A in RKO cells treated with DAG for 48 hours.

J. Immunoblot analysis of Phospho-CRAF/CRAF, Phospho-PKCα/PKC, Phospho-eIF4E/eIF4E, and HIF1A in RKO EC-R cells treated with siRNA-PKCα or siRNA-CRAF for 48 hours.

K. Immunoblot analysis of Phospho-eIF4E and eIF4E in RKO and RKO EC-R cells.

L. Immunoblot analysis of Phospho-eIF4E/eIF4E and HIF1A in RKO EC-R cells after treated with Phospho-eIF4E inhibitor (10μM) or plus DAG (10μM) for 24 hours.

M. Immunoblot analysis of Phospho-eIF4E/eIF4E and HIF1A in RKO EC-R cells treated with DAG for 48 hours.

The data were presented as the mean ± SEM of three independent experiments, ns, no significance; *$p < 0.05$, **$p < 0.01$, and ***$p < 0.001$. (2-tailed unpaired t test in G; 1-way ANOVA with Tukey's multiple-comparison test in H).

Figure 7. Reducing intratumoral DAG by Fenofibrate overcomes the resistance of *BRAF*^{V600E}-mutant mCRC tumors upon doublet therapy

A-C. Xenograft tumor size in nude mice inoculated with encorafenib-cetuximab-resistant *BRAF* ^{V600E}-mutant mCRC tumor tissues corresponding respectively treated with vehicle (PBS), encorafenib(20mg/kg), cetuximab(20mg/kg), fenofibrate (100mg/kg) alone or in combination three together (n=6) (A) tumor growth (C) in nude mice and quantified DAG level in tumor tissues (B) (n=6).

D-E. Representative images of H&E, Ki67, Oil red, and TUNEL staining (D). The quantitation of Ki67 and TUNEL (E) (n=4).

F. Immunoblot analysis of PKCα/CRAF and MEK/ERK signaling in tumor tissues related to Figure 7A.

G-H. Xenograft tumor size in nude mice inoculated with encorafenib-cetuximab-resistant *BRAF* ^{V600E}-mutant mCRC tumor tissues corresponding respectively orally treated with vehicle (PBS), encorafenib/cetuximab (20mg/kg,20mg/kg), encorafenib/cetuximab/fenofibrate (20mg/kg, 20mg/kg, 100mg/kg), encorafenib/cetuximab/fenofibrate/PMA (20mg/kg, 20mg/kg, 100mg/kg, 20mg/kg), encorafenib/cetuximab/PKC-IN-1 (20mg/kg, 20mg/kg, 30mg/kg), encorafenib/cetuximab/RAF-IN-1 (20mg/kg, 20mg/kg, 30mg/kg) (n=6)

(G) Xenograft tumor growth (H) in nude mice.

I. Western bolt assessed the protein expression of PKCα/CRAF/MEK/ERK signaling in encorafenib/cetuximab-resistant PDXs from Figure 7G. The tumor tissues were harvested for western blotting to detect the indicated signaling proteins. A representative blot was shown from three independent experiments.

The data were presented as the mean ± SEM of three independent experiments, ns, no significance; *$p < 0.05$, **$p < 0.01$, and ***$p < 0.001$. (1-way ANOVA with Tukey's multiple-comparison test in B and E; 2-way ANOVA with Tukey's multiple-comparison test in C and H).

Graphical abstract

Upregulated MOGAT3 mediates DAG accumulation through promoting DAG synthesis and reducing FAO, and then accumulated DAG drives MAPK pathway re-

activation via phosphorylation PKCα/CRAF/MEK/ERK cascade, conferred the acquired resistance in *BRAF*^{V600E}-mutant mCRC to encorafenib/cetuximab. Meanwhile, accumulated DAG-mediated PKCα/CRAF activation promotes MOGAT3 transcriptional expression through eIF4E/HIF1A signaling elevation, intensifying MOGAT3/DAG-mediated resistance status. Targeting DAG by fenofibrate or Pf-06471533 improves the treatment efficiency in resistant *BRAF* ^{V600E}-mutant mCRC to encorafenib/cetuximab therapy, depending on PKCα/CRAF axis inhibition.

References:

1. Sung H, Ferlay J, Siegel R, Laversanne M, Soerjomataram I, Jemal A, et al. Global Cancer Statistics 2020: GLOBOCAN Estimates of Incidence and Mortality Worldwide for 36 Cancers in 185 Countries. 2021;71(3):209-49.
2. Barras D. BRAF Mutation in Colorectal Cancer: An Update. *Biomark Cancer.* 2015;7(Suppl 1):9-12.
3. Sanz-Garcia E, Argiles G, Elez E, and Tabernero J. BRAF mutant colorectal cancer: prognosis, treatment, and new perspectives. *Ann Oncol.* 2017;28(11):2648-57.
4. Tabernero J, Grothey A, Van Cutsem E, Yaeger R, Wasan H, Yoshino T, et al. Encorafenib Plus Cetuximab as a New Standard of Care for Previously Treated BRAF V600E-Mutant Metastatic Colorectal Cancer: Updated Survival Results and Subgroup Analyses from the BEACON Study. *J Clin Oncol.* 2021;39(4):273-84.
5. Kopetz S, Grothey A, Yaeger R, Van Cutsem E, Desai J, Yoshino T, et al. Encorafenib,

Binimetinib, and Cetuximab in BRAF V600E-Mutated Colorectal Cancer. *N Engl J Med.* 2019;381(17):1632-43.

6. Xu T, Wang X, Wang Z, Deng T, Qi C, Liu D, et al. Molecular mechanisms underlying the resistance of BRAF V600E-mutant metastatic colorectal cancer to EGFR/BRAF inhibitors. *Ther Adv Med Oncol.* 2022;14:17588359221105022.

7. Ruiz-Saenz A, Atreya CE, Wang C, Pan B, Dreyer CA, Brunen D, et al. A reversible SRC-relayed COX2 inflammatory program drives resistance to BRAF and EGFR inhibition in BRAF(V600E) colorectal tumors. *Nat Cancer.* 2023;4(2):240-56.

8. Elez E, Ros J, Fernández J, Villacampa G, Moreno-Cárdenas AB, Arenillas C, et al. RNF43 mutations predict response to anti-BRAF/EGFR combinatory therapies in BRAF(V600E) metastatic colorectal cancer. *Nat Med.* 2022;28(10):2162-70.

9. Pavlova NN, and Thompson CB. The Emerging Hallmarks of Cancer Metabolism. *Cell Metab.* 2016;23(1):27-47.

10. Haq R, Fisher DE, and Widlund HR. Molecular pathways: BRAF induces bioenergetic adaptation by attenuating oxidative phosphorylation. *Clin Cancer Res.* 2014;20(9):2257-63.

11. Turner JA, Paton EL, Van Gulick R, Stefanoni D, Cendali F, Reisz J, et al. BRAF Modulates Lipid Use and Accumulation. *Cancers (Basel).* 2022;14(9).

12. Yosef HK, Mavarani L, Maghnouj A, Hahn S, El-Mashtoly SF, and Gerwert K. In vitro prediction of the efficacy of molecularly targeted cancer therapy by Raman spectral imaging. *Anal Bioanal Chem.* 2015;407(27):8321-31.

13. Teicher BA, Linehan WM, and Helman LJ. Targeting cancer metabolism. *Clin Cancer Res.* 2012;18(20):5537-45.

14. Fu Y, Zou T, Shen X, Nelson PJ, Li J, Wu C, et al. Lipid metabolism in cancer progression and therapeutic strategies. *MedComm (2020).* 2021;2(1):27-59.

15. Grigor MR, and Bell RM. Separate monoacylglycerol and diacylglycerol acyltransferases function in intestinal triacylglycerol synthesis. *Biochim Biophys Acta.* 1982;712(3):464-72.

16. Yang M, and Nickels JT. MOGAT2: A New Therapeutic Target for Metabolic Syndrome. *Diseases.* 2015;3(3):176-92.

17. Soufi N, Hall AM, Chen Z, Yoshino J, Collier SL, Mathews JC, et al. Inhibiting monoacylglycerol acyltransferase 1 ameliorates hepatic metabolic abnormalities but not inflammation and injury in mice. *J Biol Chem.* 2014;289(43):30177-88.

18. Cheng D, Nelson TC, Chen J, Walker SG, Wardwell-Swanson J, Meegalla R, et al. Identification of acyl coenzyme A:monoacylglycerol acyltransferase 3, an intestinal specific enzyme implicated in dietary fat absorption. *J Biol Chem.* 2003;278(16):13611-4.

19. Yao YM, Donoho GP, Iversen PW, Zhang Y, Van Horn RD, Forest A, et al. Mouse PDX Trial Suggests Synergy of Concurrent Inhibition of RAF and EGFR in Colorectal Cancer with BRAF or KRAS Mutations. *Clin Cancer Res.* 2017;23(18):5547-60.

20. McLelland G-L, Lopez-Osias M, Verzijl CRC, Ellenbroek BD, Oliveira RA, Boon NJ, et al. Identification of an alternative triglyceride biosynthesis pathway. *Nature.* 2023;621(7977):171-8.

21. Cao J, Cheng L, and Shi Y. Catalytic properties of MGAT3, a putative triacylgycerol synthase. *J Lipid Res.* 2007;48(3):583-91.

22. Khatun I, Clark RW, Vera NB, Kou K, Erion DM, Coskran T, et al. Characterization of a Novel Intestinal Glycerol-3-phosphate Acyltransferase Pathway and Its Role in Lipid Homeostasis. *J*

Biol Chem. 2016;291(6):2602-15.

23. Ahronian LG, Sennott EM, Van Allen EM, Wagle N, Kwak EL, Faris JE, et al. Clinical Acquired Resistance to RAF Inhibitor Combinations in BRAF-Mutant Colorectal Cancer through MAPK Pathway Alterations. *Cancer Discov.* 2015;5(4):358-67.

24. Griner EM, and Kazanietz MG. Protein kinase C and other diacylglycerol effectors in cancer. *Nat Rev Cancer.* 2007;7(4):281-94.

25. Strickler JH, Wu C, and Bekaii-Saab T. Targeting BRAF in metastatic colorectal cancer: Maximizing molecular approaches. *Cancer Treat Rev.* 2017;60:109-19.

26. Kolch W, Heidecker G, Kochs G, Hummel R, Vahidi H, Mischak H, et al. Protein kinase C alpha activates RAF-1 by direct phosphorylation. *Nature.* 1993;364(6434):249-52.

27. Lin SC, Liao WL, Lee JC, and Tsai SJ. Hypoxia-regulated gene network in drug resistance and cancer progression. *Exp Biol Med (Maywood).* 2014;239(7):779-92.

28. Yuan Y, Tan L, Wang L, Zou D, Liu J, Lu X, et al. The Expression Pattern of Hypoxia-Related Genes Predicts the Prognosis and Mediates Drug Resistance in Colorectal Cancer. *Front Cell Dev Biol.* 2022;10:814621.

29. Rohwer N, and Cramer T. Hypoxia-mediated drug resistance: novel insights on the functional interaction of HIFs and cell death pathways. *Drug Resist Updat.* 2011;14(3):191-201.

30. Chen Z, Han F, Du Y, Shi H, and Zhou W. Hypoxic microenvironment in cancer: molecular mechanisms and therapeutic interventions. *Signal Transduct Target Ther.* 2023;8(1):70.

31. Semenza GL. Targeting HIF-1 for cancer therapy. *Nat Rev Cancer.* 2003;3(10):721-32.

32. Karni R, Dor Y, Keshet E, Meyuhas O, and Levitzki A. Activated pp60c-Src leads to elevated hypoxia-inducible factor (HIF)-1alpha expression under normoxia. *J Biol Chem.*

2002;277(45):42919-25.

33. Superko HR. A review of combined hyperlipidaemia and its treatment with fenofibrate. *J Int Med Res.* 1989;17(2):99-112.

34. Carrasco S, and Merida I. Diacylglycerol, when simplicity becomes complex. *Trends Biochem Sci.* 2007;32(1):27-36.

35. Eichmann TO, and Lass A. DAG tales: the multiple faces of diacylglycerol--stereochemistry, metabolism, and signaling. *Cell Mol Life Sci.* 2015;72(20):3931-52.

36. Kolczynska K, Loza-Valdes A, Hawro I, and Sumara G. Diacylglycerol-evoked activation of PKC and PKD isoforms in regulation of glucose and lipid metabolism: a review. *Lipids Health Dis.* 2020;19(1):113.

37. Torres-Ayuso P, Tello-Lafoz M, Merida I, and Avila-Flores A. Diacylglycerol kinase-zeta regulates mTORC1 and lipogenic metabolism in cancer cells through SREBP-1. *Oncogenesis.* 2015;4(8):e164.

38. Xu S, Tang J, Wang C, Liu J, Fu Y, and Luo Y. CXCR7 promotes melanoma tumorigenesis via Src kinase signaling. *Cell Death Dis.* 2019;10(3):191.

39. Zhao Y, Xing C, Deng Y, Ye C, and Peng H. HIF-1α signaling: Essential roles in tumorigenesis and implications in targeted therapies. *Genes Dis.* 2024;11(1):234-51.

40. Nagao A, Kobayashi M, Koyasu S, Chow CCT, and Harada H. HIF-1-Dependent Reprogramming of Glucose Metabolic Pathway of Cancer Cells and Its Therapeutic Significance. *Int J Mol Sci.* 2019;20(2).

41. Bensaad K, Favaro E, Lewis CA, Peck B, Lord S, Collins JM, et al. Fatty acid uptake and lipid storage induced by HIF-1α contribute to cell growth and survival after hypoxia-reoxygenation.

Cell Rep. 2014;9(1):349-65.

42. Seo J, Jeong D-W, Park J-W, Lee K-W, Fukuda J, and Chun Y-S. Fatty-acid-induced FABP5/HIF-1 reprograms lipid metabolism and enhances the proliferation of liver cancer cells. *Communications Biology.* 2020;3(1):638.

43. Krepler C, Xiao M, Sproesser K, Brafford PA, Shannan B, Beqiri M, et al. Personalized Preclinical Trials in BRAF Inhibitor-Resistant Patient-Derived Xenograft Models Identify Second-Line Combination Therapies. *Clin Cancer Res.* 2016;22(7):1592-602.

44. Yang H, Higgins B, Kolinsky K, Packman K, Bradley WD, Lee RJ, et al. Antitumor activity of BRAF inhibitor vemurafenib in preclinical models of BRAF-mutant colorectal cancer. *Cancer Res.* 2012;72(3):779-89.

45. Geng F, Cheng X, Wu X, Yoo JY, Cheng C, Guo JY, et al. Inhibition of SOAT1 Suppresses Glioblastoma Growth via Blocking SREBP-1-Mediated Lipogenesis. *Clin Cancer Res.* 2016;22(21):5337-48.

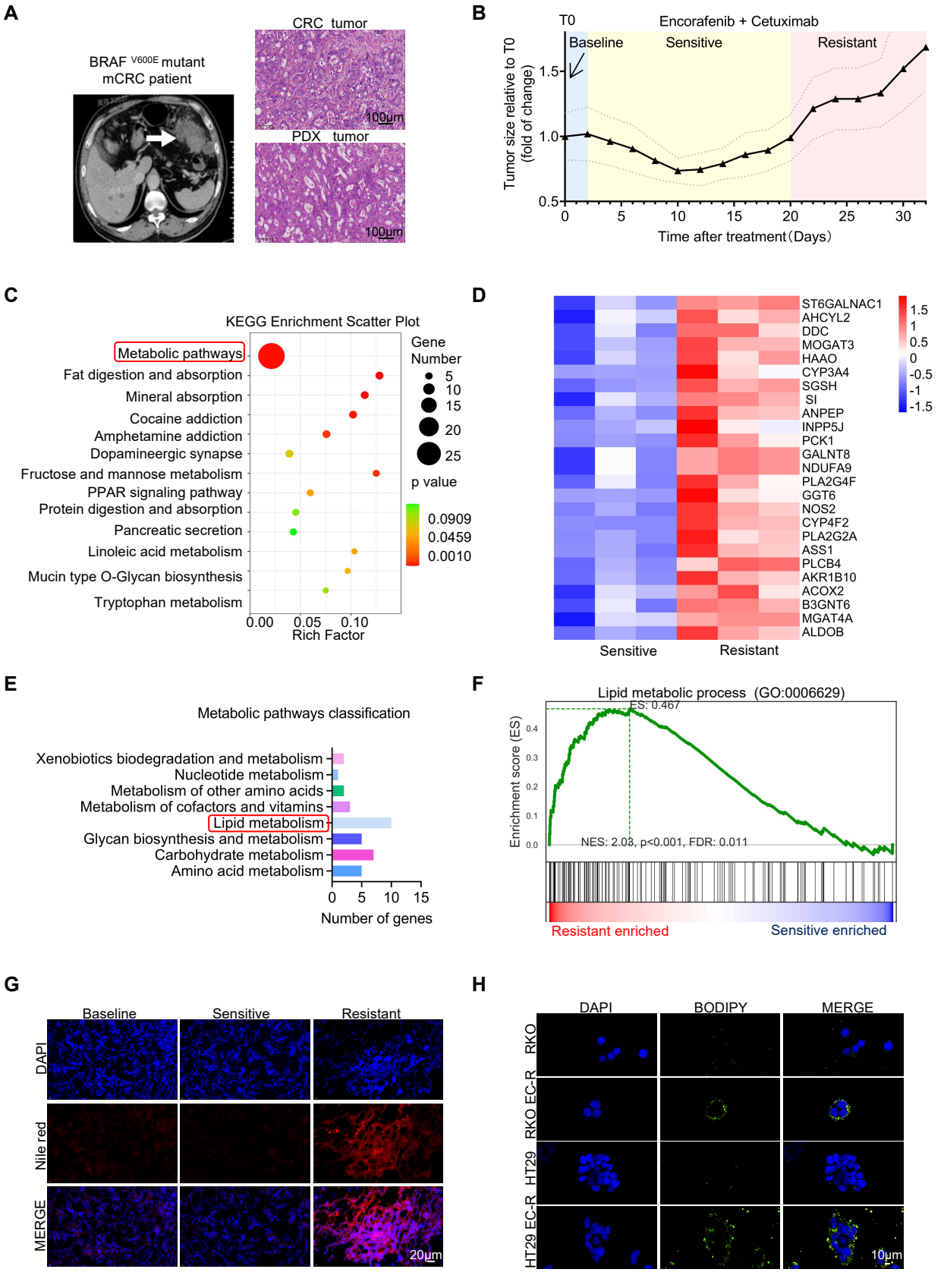
A
BRAF V600E mutant
mCRC patient
CRC tumor
100μm
PDX tumor
100μm
B
T0
Encorafenib + Cetuximab
Baseline
Sensitive
Resistant
Tumor size relative to T0
(fold of change)
Time after treatment (Days)
C
KEGG Enrichment Scatter Plot
Metabolic pathways
Fat digestion and absorption
Mineral absorption
Cocaine addiction
Amphetamine addiction
Dopaminergic synapse
Fructose and mannose metabolism
PPAR signaling pathway
Protein digestion and absorption
Pancreatic secretion
Linoleic acid metabolism
Mucin type O-Glycan biosynthesis
Tryptophan metabolism
Rich Factor
Gene Number
p value
D
ST6GALNAC1
AHCYL2
DDC
MOGAT3
HAAO
CYP3A4
SGSH
SI
ANPEP
INPP5J
PCK1
GALNT8
NDUFA9
PLA2G4F
GGT6
NOS2
CYP4F2
PLA2G2A
ASS1
PLCB4
AKR1B10
ACOX2
B3GNT6
MGAT4A
ALDOB
Sensitive
Resistant
E
Metabolic pathways classification
Xenobiotics biodegradation and metabolism
Nucleotide metabolism
Metabolism of other amino acids
Metabolism of cofactors and vitamins
Lipid metabolism
Glycan biosynthesis and metabolism
Carbohydrate metabolism
Amino acid metabolism
Number of genes
F
Lipid metabolic process (GO:0006629)
ES: 0.467
Enrichment score (ES)
NES: 2.03, p<0.001, FDR: 0.011
Resistant enriched
Sensitive enriched
G
Baseline
Sensitive
Resistant
DAPI
Nile red
MERGE
20μm
H
DAPI
BODIPY
MERGE
RKO
RKO EC-R
HT29
HT29 EC-R
10μm

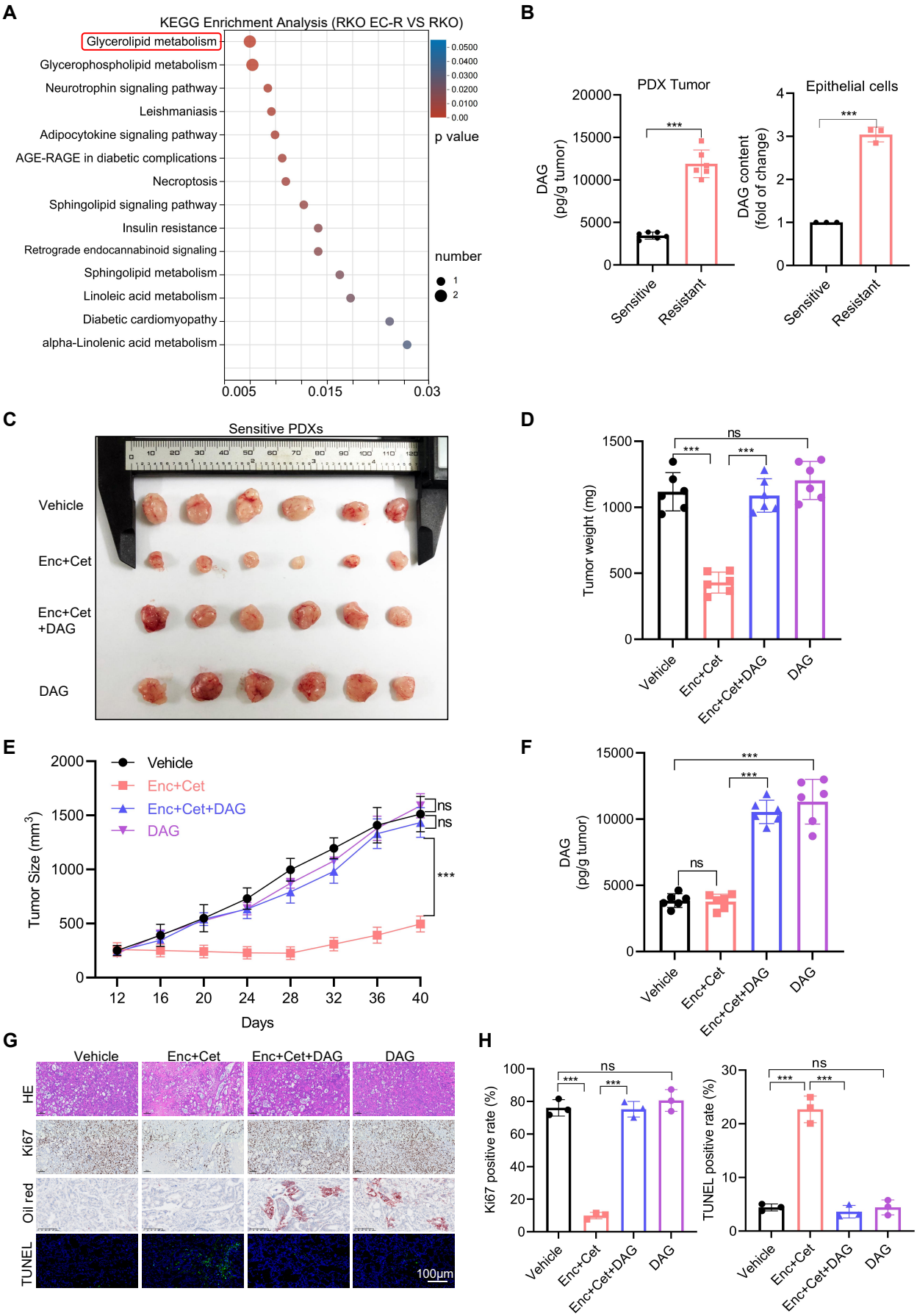
A
KEGG Enrichment Analysis (RKO EC-R VS RKO)
Glycerolipid metabolism
Glycerophospholipid metabolism
Neurotrophin signaling pathway
Leishmaniasis
Adipocytokine signaling pathway
AGE-RAGE in diabetic complications
Necroptosis
Sphingolipid signaling pathway
Insulin resistance
Retrograde endocannabinoid signaling
Sphingolipid metabolism
Linoleic acid metabolism
Diabetic cardiomyopathy
alpha-Linolenic acid metabolism
0.005
0.015
0.03
p value
number
B
PDX Tumor
Epithelial cells
DAG (pg/g tumor)
DAG content (fold of change)
Sensitive
Resistant
C
Sensitive PDXs
Vehicle
Enc+Cet
Enc+Cet +DAG
DAG
D
Tumor weight (mg)
Vehicle
Enc+Cet
Enc+Cet+DAG
DAG
E
Tumor Size (mm3)
Days
F
DAG (pg/g tumor)
G
HE
Ki67
Oil red
TUNEL
100μm
H
Ki67 positive rate (%)
TUNEL positive rate (%)

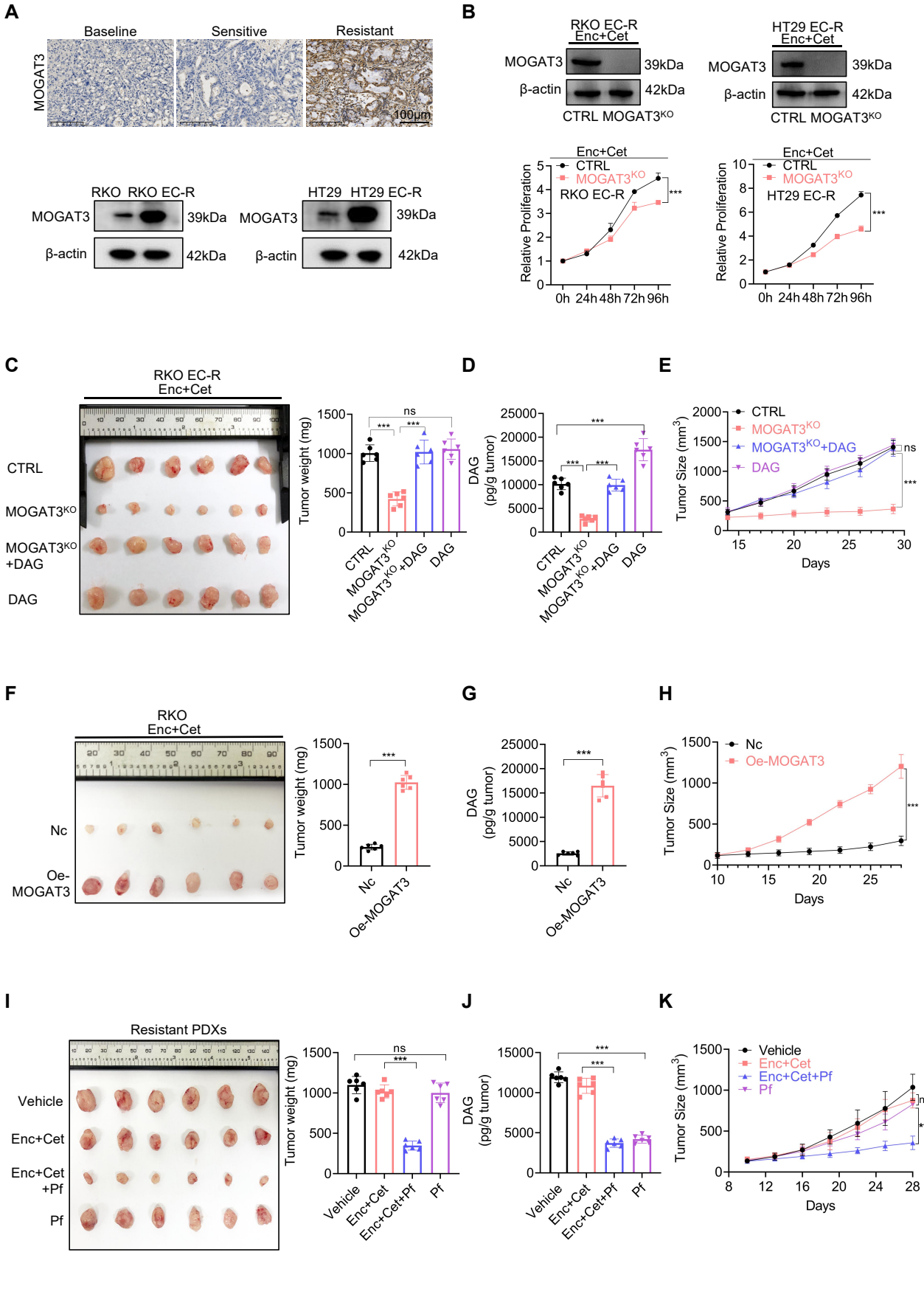
A
Baseline
Sensitive
Resistant
MOGAT3
100μm
RKO RKO EC-R
MOGAT3
39kDa
β-actin
42kDa
HT29 HT29 EC-R
MOGAT3
39kDa
β-actin
42kDa
B
RKO EC-R
Enc+Cet
MOGAT3
39kDa
β-actin
42kDa
CTRL MOGAT3KO
HT29 EC-R
Enc+Cet
MOGAT3
39kDa
β-actin
42kDa
CTRL MOGAT3KO
Enc+Cet
CTRL
MOGAT3KO
RKO EC-R
Relative Proliferation
0h 24h 48h 72h 96h
***
Enc+Cet
CTRL
MOGAT3KO
HT29 EC-R
Relative Proliferation
0h 24h 48h 72h 96h
***
C
RKO EC-R
Enc+Cet
CTRL
MOGAT3KO
MOGAT3KO +DAG
DAG
Tumor weight (mg)
ns
***
***
CTRL
MOGAT3KO
MOGAT3KO +DAG
DAG
D
DAG (pg/g tumor)
***
***
***
CTRL
MOGAT3KO
MOGAT3KO +DAG
DAG
E
Tumor Size (mm3)
CTRL
MOGAT3KO
MOGAT3KO+DAG
DAG
ns
***
Days
F
RKO
Enc+Cet
Nc
Oe-MOGAT3
Tumor weight (mg)
***
Nc
Oe-MOGAT3
G
DAG (pg/g tumor)
***
Nc
Oe-MOGAT3
H
Tumor Size (mm3)
Nc
Oe-MOGAT3
***
Days
I
Resistant PDXs
Vehicle
Enc+Cet
Enc+Cet +Pf
Pf
Tumor weight (mg)
ns
***
Vehicle
Enc+Cet
Enc+Cet+Pf
Pf
J
DAG (pg/g tumor)
***
***
Vehicle
Enc+Cet
Enc+Cet+Pf
Pf
K
Tumor Size (mm3)
Vehicle
Enc+Cet
Enc+Cet+Pf
Pf
ns
***
Days

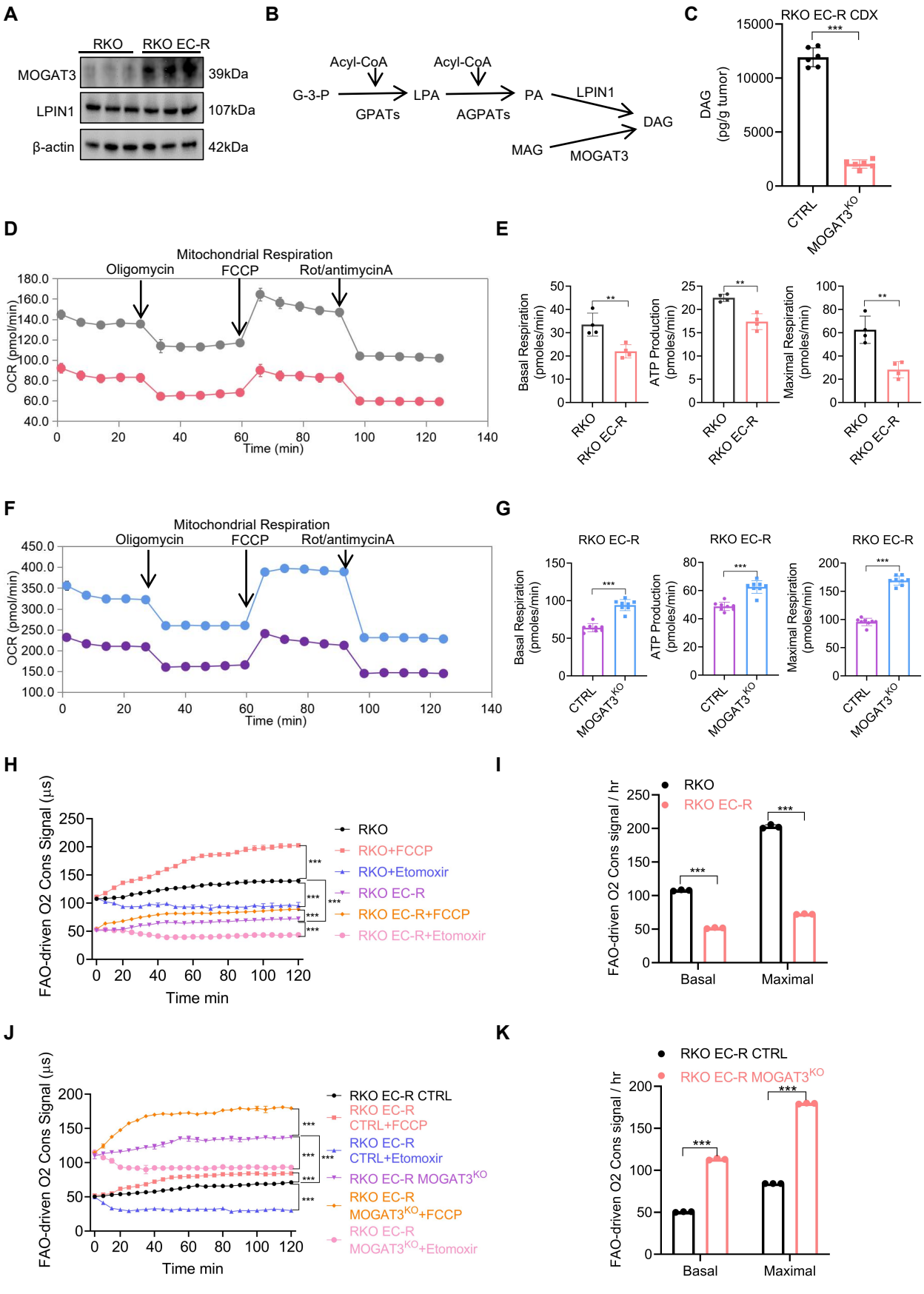
A
RKO
RKO EC-R
MOGAT3
LPIN1
β-actin
39kDa
107kDa
42kDa
B
Acyl-CoA
Acyl-CoA
G-3-P
GPATs
LPA
AGPATs
PA
LPIN1
DAG
MAG
MOGAT3
C
RKO EC-R CDX
DAG (pg/g tumor)
CTRL
MOGAT3KO
D
Mitochondrial Respiration
Oligomycin
FCCP
Rot/antimycinA
OCR (pmol/min)
Time (min)
E
Basal Respiration (pmoles/min)
ATP Production (pmoles/min)
Maximal Respiration (pmoles/min)
RKO
RKO EC-R
F
Mitochondrial Respiration
Oligomycin
FCCP
Rot/antimycinA
OCR (pmol/min)
Time (min)
G
RKO EC-R
Basal Respiration (pmoles/min)
ATP Production (pmoles/min)
Maximal Respiration (pmoles/min)
CTRL
MOGAT3KO
H
FAO-driven O2 Cons Signal (μs)
Time min
RKO
RKO+FCCP
RKO+Etomoxir
RKO EC-R
RKO EC-R+FCCP
RKO EC-R+Etomoxir
I
RKO
RKO EC-R
FAO-driven O2 Cons signal / hr
Basal
Maximal
J
FAO-driven O2 Cons Signal (μs)
Time min
RKO EC-R CTRL
RKO EC-R CTRL+FCCP
RKO EC-R CTRL+Etomoxir
RKO EC-R MOGAT3KO
RKO EC-R MOGAT3KO+FCCP
RKO EC-R MOGAT3KO+Etomoxir
K
RKO EC-R CTRL
RKO EC-R MOGAT3KO
FAO-driven O2 Cons signal / hr
Basal
Maximal

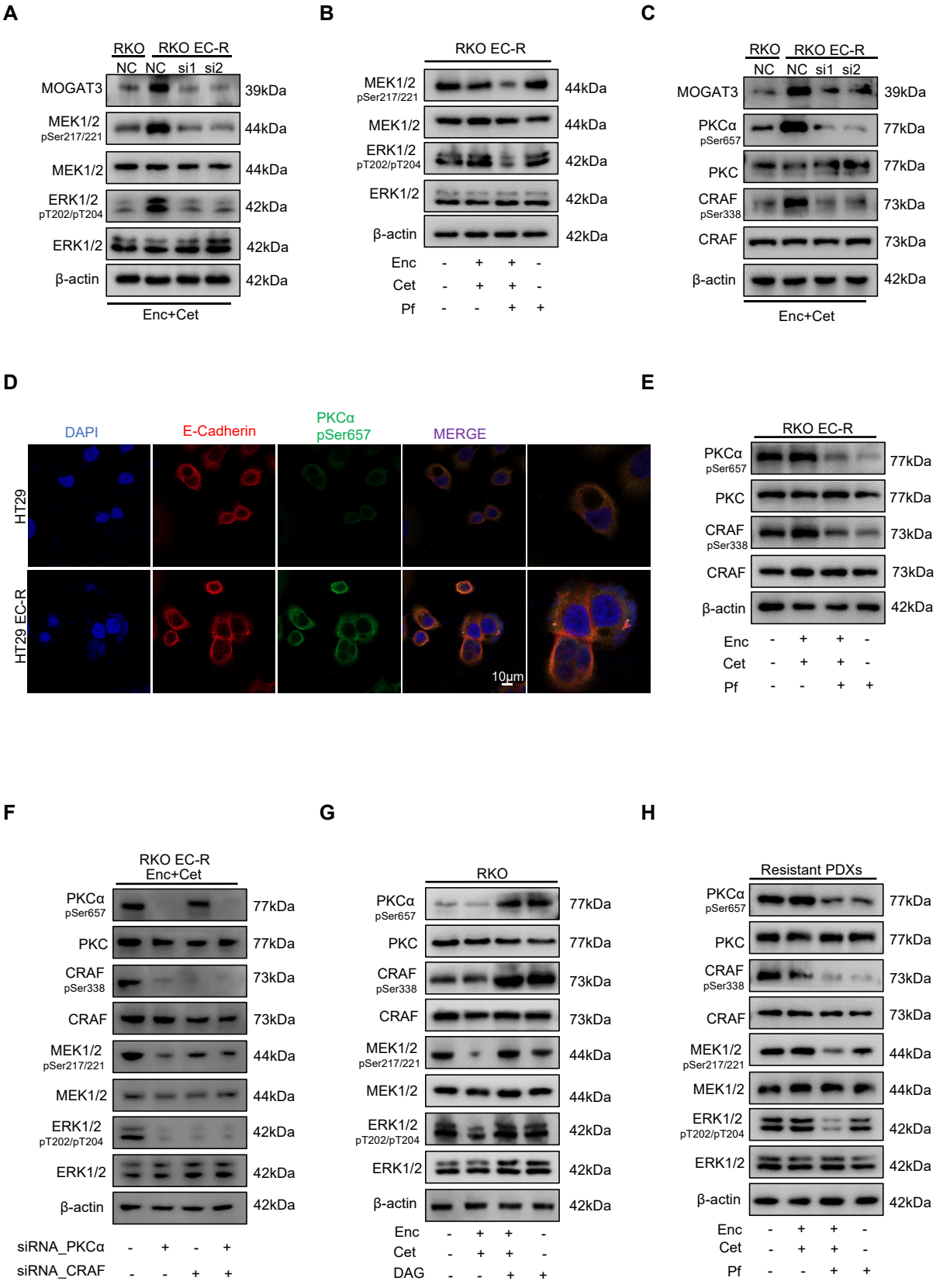
A
RKO
RKO EC-R
NC NC si1 si2
MOGAT3 39kDa
MEK1/2 pSer217/221 44kDa
MEK1/2 44kDa
ERK1/2 pT202/pT204 42kDa
ERK1/2 42kDa
β-actin 42kDa
Enc+Cet
B
RKO EC-R
MEK1/2 pSer217/221 44kDa
MEK1/2 44kDa
ERK1/2 pT202/pT204 42kDa
ERK1/2 42kDa
β-actin 42kDa
Enc - + + -
Cet - + + -
Pf - - + +
C
RKO
RKO EC-R
NC NC si1 si2
MOGAT3 39kDa
PKCα pSer657 77kDa
PKC 77kDa
CRAF pSer338 73kDa
CRAF 73kDa
β-actin 42kDa
Enc+Cet
D
DAPI
E-Cadherin
PKCα pSer657
MERGE
HT29
HT29 EC-R
10μm
E
RKO EC-R
PKCα pSer657 77kDa
PKC 77kDa
CRAF pSer338 73kDa
CRAF 73kDa
β-actin 42kDa
Enc - + + -
Cet - + + -
Pf - - + +
F
RKO EC-R
Enc+Cet
PKCα pSer657 77kDa
PKC 77kDa
CRAF pSer338 73kDa
CRAF 73kDa
MEK1/2 pSer217/221 44kDa
MEK1/2 44kDa
ERK1/2 pT202/pT204 42kDa
ERK1/2 42kDa
β-actin 42kDa
siRNA_PKCα - + - +
siRNA_CRAF - - + +
G
RKO
PKCα pSer657 77kDa
PKC 77kDa
CRAF pSer338 73kDa
CRAF 73kDa
MEK1/2 pSer217/221 44kDa
MEK1/2 44kDa
ERK1/2 pT202/pT204 42kDa
ERK1/2 42kDa
β-actin 42kDa
Enc - + + -
Cet - + + -
DAG - - + +
H
Resistant PDXs
PKCα pSer657 77kDa
PKC 77kDa
CRAF pSer338 73kDa
CRAF 73kDa
MEK1/2 pSer217/221 44kDa
MEK1/2 44kDa
ERK1/2 pT202/pT204 42kDa
ERK1/2 42kDa
β-actin 42kDa
Enc - + + -
Cet - + + -
Pf - - + +

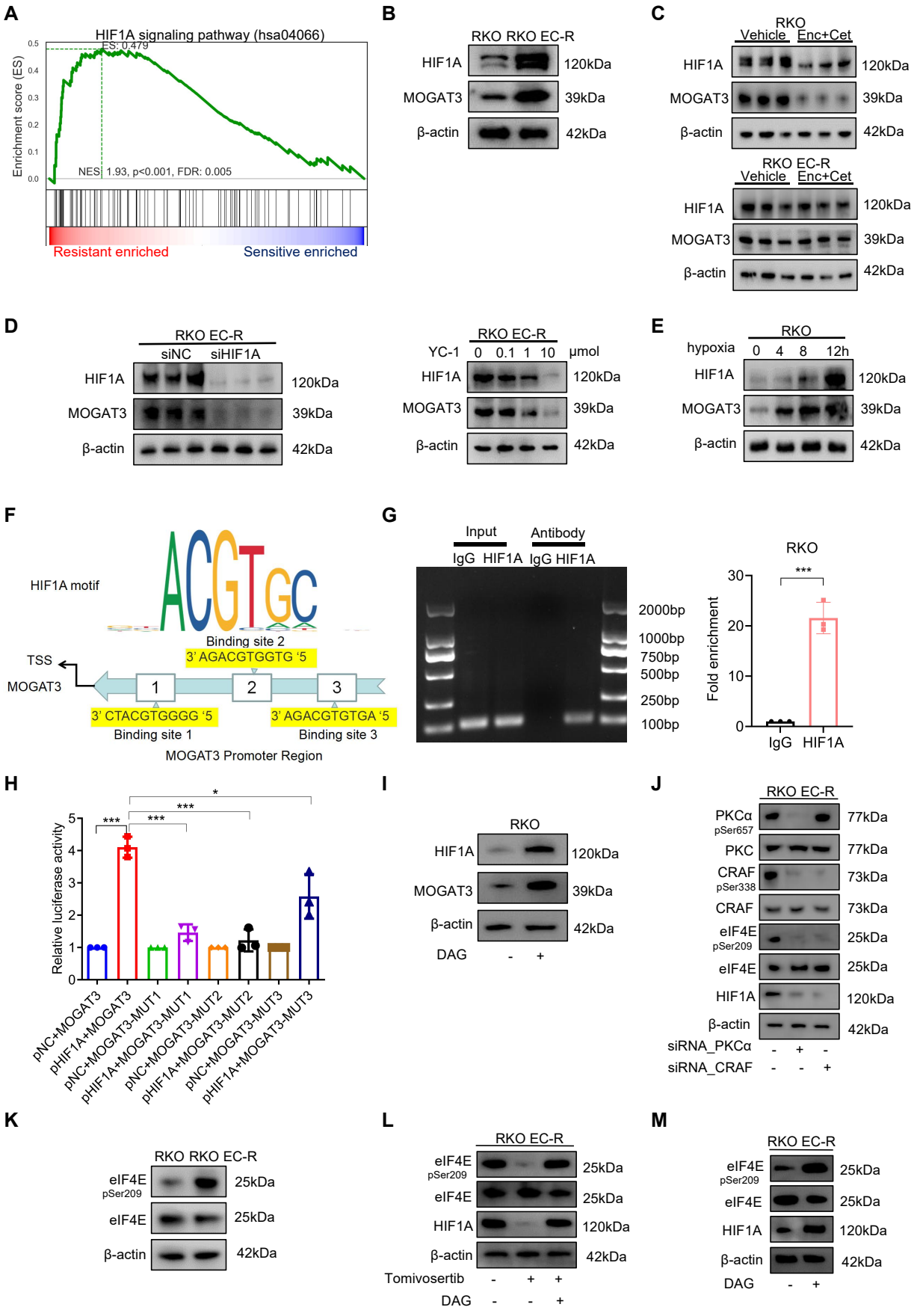
A
HIF1A signaling pathway (hsa04066)
ES: 0.479
Enrichment score (ES)
NES: 1.93, p<0.001, FDR: 0.005
Resistant enriched
Sensitive enriched
B
RKO RKO EC-R
HIF1A
MOGAT3
β-actin
120kDa
39kDa
42kDa
C
RKO
Vehicle Enc+Cet
RKO EC-R
Vehicle Enc+Cet
D
RKO EC-R
siNC siHIF1A
YC-1 0 0.1 1 10 μmol
E
RKO
hypoxia 0 4 8 12h
F
HIF1A motif
Binding site 2
3' AGACGTGGTG '5
TSS
MOGAT3
3' CTACGTGGGG '5
3' AGACGTGTGA '5
Binding site 1
Binding site 3
MOGAT3 Promoter Region
G
Input
Antibody
IgG HIF1A IgG HIF1A
2000bp
1000bp
750bp
500bp
250bp
100bp
RKO
Fold enrichment
IgG HIF1A
H
Relative luciferase activity
pNC+MOGAT3
pHIF1A+MOGAT3
pNC+MOGAT3-MUT1
pHIF1A+MOGAT3-MUT1
pNC+MOGAT3-MUT2
pHIF1A+MOGAT3-MUT2
pNC+MOGAT3-MUT3
pHIF1A+MOGAT3-MUT3
I
RKO
DAG
J
RKO EC-R
PKCα pSer657
PKC
CRAF pSer338
CRAF
eIF4E pSer209
eIF4E
77kDa
73kDa
25kDa
siRNA_PKCα
siRNA_CRAF
K
RKO RKO EC-R
L
RKO EC-R
Tomivosertib
DAG
M
RKO EC-R
DAG

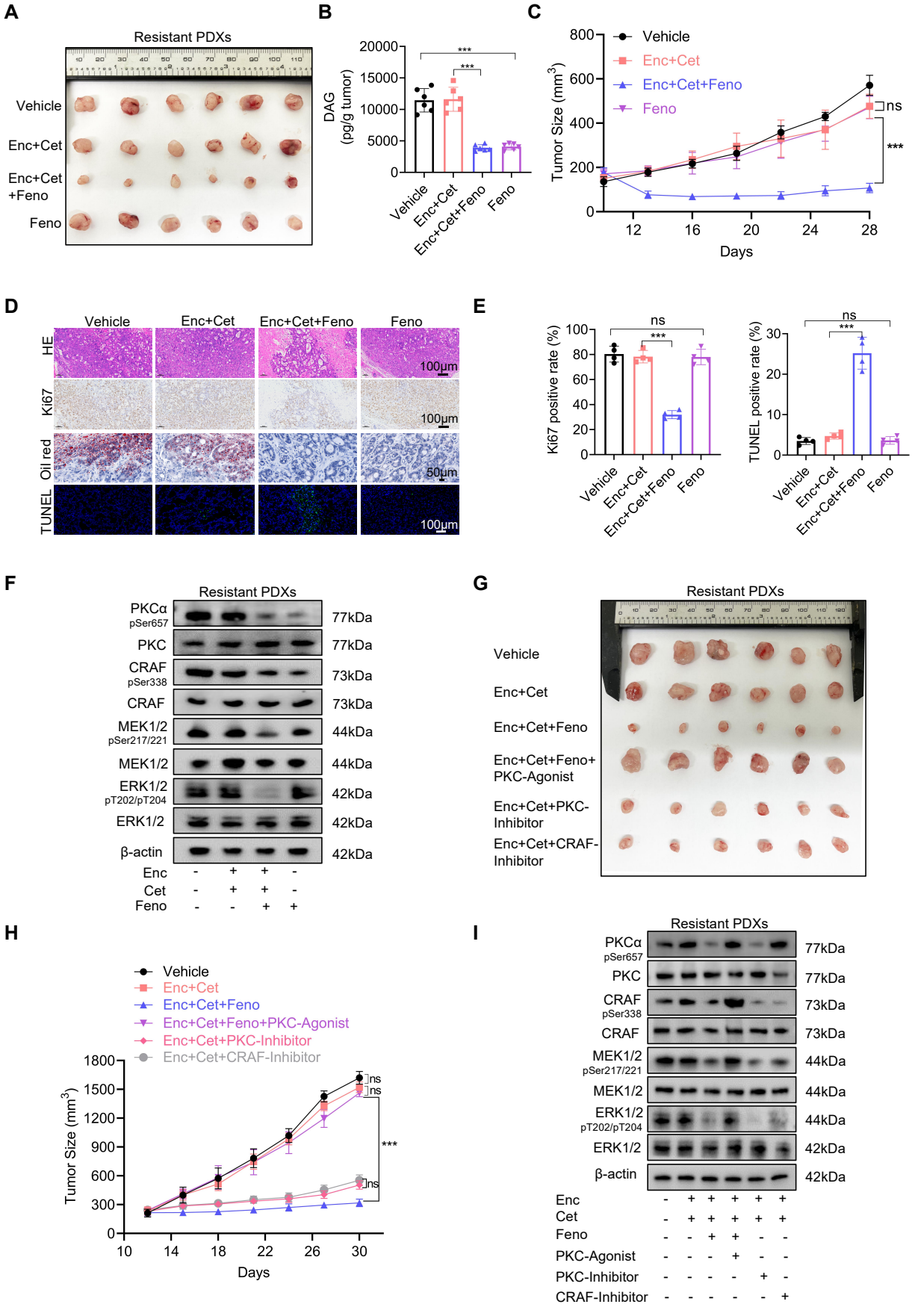
A
Resistant PDXs
Vehicle
Enc+Cet
Enc+Cet +Feno
Feno
B
DAG (pg/g tumor)
20000
15000
10000
5000
0
***
***
Vehicle
Enc+Cet
Enc+Cet+Feno
Feno
C
Tumor Size (mm3)
800
600
400
200
0
Vehicle
Enc+Cet
Enc+Cet+Feno
Feno
ns
***
12
16
20
24
28
Days
D
Vehicle
Enc+Cet
Enc+Cet+Feno
Feno
HE
Ki67
Oil red
TUNEL
100μm
100μm
50μm
100μm
E
Ki67 positive rate (%)
100
80
60
40
20
0
ns
***
Vehicle
Enc+Cet
Enc+Cet+Feno
Feno
TUNEL positive rate (%)
30
20
10
0
ns
***
Vehicle
Enc+Cet
Enc+Cet+Feno
Feno
F
Resistant PDXs
PKCα pSer657
77kDa
PKC
77kDa
CRAF pSer338
73kDa
CRAF
73kDa
MEK1/2 pSer217/221
44kDa
MEK1/2
44kDa
ERK1/2 pT202/pT204
42kDa
ERK1/2
42kDa
β-actin
42kDa
Enc - + + -
Cet - + + -
Feno - - + +
G
Resistant PDXs
Vehicle
Enc+Cet
Enc+Cet+Feno
Enc+Cet+Feno+ PKC-Agonist
Enc+Cet+PKC-Inhibitor
Enc+Cet+CRAF-Inhibitor
H
Vehicle
Enc+Cet
Enc+Cet+Feno
Enc+Cet+Feno+PKC-Agonist
Enc+Cet+PKC-Inhibitor
Enc+Cet+CRAF-Inhibitor
Tumor Size (mm3)
1800
1500
1200
900
600
300
0
ns
ns
***
ns
10
14
18
22
26
30
Days
I
Resistant PDXs
PKCα pSer657
77kDa
PKC
77kDa
CRAF pSer338
73kDa
CRAF
73kDa
MEK1/2 pSer217/221
44kDa
MEK1/2
44kDa
ERK1/2 pT202/pT204
44kDa
ERK1/2
42kDa
β-actin
42kDa
Enc - + + + + +
Cet - + + + + +
Feno - - + + - -
PKC-Agonist - - - + - -
PKC-Inhibitor - - - - + -
CRAF-Inhibitor - - - - - +